THE *SPITZER* c2d SURVEY OF LARGE, NEARBY, INTERSTELLAR CLOUDS. VI. PERSEUS OBSERVED WITH MIPS

L. M. Rebull,[1] K. R. Stapelfeldt,[2] N. J. Evans II,[3] J. K. Jørgensen,[4] P. M. Harvey,[3] T. Y. Brooke,[5]
T. L. Bourke,[4] D. L. Padgett,[1] N. L. Chapman,[6] S.-P. Lai,[6,7,8] W. J. Spiesman,[3] A. Noriega-Crespo,[1]
B. Merín,[9] T. Huard,[4] L. E. Allen,[4] G. A. Blake,[10] T. Jarrett,[11] D. W. Koerner,[12]
L. G. Mundy,[6] P. C. Myers,[4] A. I. Sargent,[5] E. F. van Dishoeck,[9]
Z. Wahhaj,[12] and K. E. Young[3,13]

Received 2006 August 9; accepted 2007 January 23

ABSTRACT

We present observations of 10.6 deg^2 of the Perseus molecular cloud at 24, 70, and 160 μm with *Spitzer* MIPS. The images show prominent, complex extended emission dominated by illuminating B stars on the east side of the cloud and by cold filaments of 160 μm emission on the west side. Of 3950 point sources identified at 24 μm, 1141 have 2MASS counterparts. A quarter of these populate regions of the K_s versus $K_s - [24]$ diagram that are distinct from stellar photospheres and background galaxies and thus are likely to be cloud members with infrared excess. Nearly half (46%) of these 24 μm excess sources are distributed outside the IC 348 and NGC 1333 clusters. A significant number of *IRAS* PSC objects are not recovered by *Spitzer* MIPS, most often because the *IRAS* objects were confused by bright nebulosity. The intercluster region contains several tightly clumped ($r \sim 0.1$ pc) young stellar aggregates whose members exhibit a wide variety of infrared SEDs characteristic of different circumstellar environments. This could be explained by a significant age spread among the aggregate members, or if the members formed at the same time, a remarkably rapid circumstellar evolution would be required to account for the association of Class I and Class III sources at ages ≲1 Myr. We highlight important results for the HH 211 flow, where the bow shocks are detected at both 24 and 70 μm, and for the debris disk candidate BD +31 643, where the MIPS data show the linear nebulosity to be an unrelated interstellar feature. Our data, mosaics, and catalogs are available at the *Spitzer* Science Archive for use by interested members of the community.

Subject headings: circumstellar matter — infrared: ISM — infrared: stars — ISM: clouds —
ISM: individual (IC 348, NGC 1333) — ISM: jets and outflows —
stars: formation — stars: pre–main-sequence

1. INTRODUCTION

The *Spitzer Space Telescope* Legacy program "From Molecular Cores to Planet-forming Disks" (c2d; Evans et al. 2003) selected five large star-forming clouds for mapping with the Infrared Array Camera (IRAC, 3.6, 4.5, 5.8, and 8 μm; Fazio et al. 2004) and the Multiband Imaging Photometer for *Spitzer* (MIPS, 24, 70, and 160 μm; Rieke et al. 2004). These clouds were selected to be within 350 pc, to have a substantial mass of molecular gas, and to have a range of cloud properties, thereby allowing studies of star formation in isolation, in groups, and in clusters. The goals of this aspect of the c2d project (for more information see Evans et al. 2003) include determining the stellar content of the clouds, the distributions of the youngest stars and substellar objects, and the properties of their disks and envelopes. All of these *Spitzer* cloud studies represent the first unbiased mid-infrared (MIR) surveys across entire clouds at this sensitivity and spatial resolution, where in the past only targeted, small field-of-view observations have been possible.

Perseus is one of five nearby star-forming clouds mapped with IRAC and MIPS by c2d, also including Chamaeleon II, Lupus I, III, and IV, Ophiuchus, and Serpens (for an overview see Evans et al. 2003). Previous papers in this series presented IRAC observations of Serpens (Harvey et al. 2006), Perseus (Jørgensen et al. 2006, hereafter J06), and Chamaeleon II (Porras et al. 2007) and MIPS observations of Chamaeleon II (Young et al. 2005) and Lupus I, III, and IV (Chapman et al. 2007).

The Perseus molecular cloud is a source of active star formation with few high-mass stars, none earlier than early B. While nowhere near as chaotic as the Orion star-forming region, it is also not as quiescent as the Taurus molecular cloud, and so provides an "intermediate" case study. IC 348 and NGC 1333 are the two densest and most famous star-forming clusters in this region, containing numerous stars <1–2 Myr old. Ongoing star formation is certainly occurring throughout the cloud, including in named regions such as L1448 and B5; there are deeply embedded Class 0 objects found outside the two major clusters (see, e.g., J06).

[1] *Spitzer* Science Center, California Institute of Technology, Pasadena, CA 91125; luisa.rebull@jpl.nasa.gov.

[2] Jet Propulsion Laboratory, California Institute of Technology, Pasadena, CA 91109.

[3] Department of Astronomy, University of Texas, Austin, TX 78712.

[4] Harvard-Smithsonian Center for Astrophysics, Cambridge, MA 02138.

[5] Division of Physics, Mathematics, and Astronomy, California Institute of Technology, Pasadena, CA 91125.

[6] Department of Astronomy, University of Maryland, College Park, MD 20742.

[7] Institute of Astronomy and Department of Physics, National Tsing Hua University, Hsinchu 30043, Taiwan.

[8] Academia Sinica Institute of Astronomy and Astrophysics, Taipei 106, Taiwan.

[9] Leiden Observatory, NL 2300 RA Leiden, Netherlands.

[10] Division of Geological and Planetary Sciences, California Institute of Technology, Pasadena, CA 91125.

[11] Infrared Processing and Analysis Center, California Institute of Technology, Pasadena, CA 91125.

[12] Department of Physics and Astronomy, Northern Arizona University, Flagstaff, AZ 86011-6010.

[13] Department of Physical Sciences, Nicholls State University, Thibodaux, LA 70301.

The Perseus cloud is large enough that different parts of it may be at significantly different distances; see the discussion in Enoch et al. (2006). Following that paper and J06, we take the distance to Perseus to be 250 pc, although we acknowledge that there may indeed be a substantial distance gradient across the cloud, or there might even be multiple pieces located at several different distances.

The Perseus cloud is rich in both point sources and complex extended emission. *IRAS* observations revealed more than 200 apparent point sources and complex interstellar medium (ISM) structures, including a large ring thought to be an H II region, G159.6−18.5, excited by HD 278942 (Andersson et al. 2000). Ridge et al. (2006) argue that the ring is *behind* the main Perseus cloud. Hatchell et al. (2005) find via a survey at 850 and 450 μm a high degree of point-source clustering and filamentary structures throughout the cloud. Enoch et al. (2006) also find strong point-source clustering in their 1.1 mm continuum survey. The *Spitzer* IRAC study of Perseus by J06 concluded that (1) there are significant numbers of stars being formed outside of the two main clusters (IC 348 and NGC 1333); (2) the fraction of Class I, Class II, and "flat-spectrum" young stellar objects (YSOs) differs between the two rich clusters and the extended cloud population; and (3) deeply embedded Class 0 objects are detected, with very red $[3.6] − [4.5]$ colors (but not similarly red $[5.8] − [8]$ colors).

MIPS observations at 24 μm ($\sim 6''$ resolution), 70 μm ($\sim 20''$ resolution), and 160 μm ($\sim 40''$ resolution) can elucidate many aspects of the ongoing star formation in Perseus. Although the emission from stellar photospheres is falling rapidly at 24 μm, emission from circumstellar material makes many of the young cluster members still quite bright at 24 μm, so MIPS finds the young stars easily. Emission from the cloud itself becomes increasingly prominent in the MIPS 24, 70, and 160 μm bands, allowing dusty molecular material in the temperature range 120–20 K to be probed. MIPS reveals complex extended emission throughout the Perseus region at all three of its wavelengths.

This paper presents MIPS data covering more than 10.5 deg^2 in Perseus. We also use information obtained from the IRAC data for Perseus from J06. As a result of observational constraints (see § 2), the IRAC data cover only about one-third the area of the MIPS data (IRAC covers 3.86 deg^2), so we use the IRAC data where possible, but large areas of our map have no IRAC data at all.

The goals of this paper are to present the MIPS data in a format similar to that found in the other papers in the series, to discuss some of the high-level conclusions drawn from these data, and to highlight some of the interesting objects we have found. Because this paper is part of a series, there is synergy with both the papers that have gone before and those to come. Because the IRAC data, where they exist, are usually important for understanding the objects seen in the Perseus map, there are extensive references to J06; for example, spectral energy distributions (SEDs) for some objects discussed there were deferred to this paper for presentation. Similarly, there are references to future work throughout this paper. One such future paper will present a complete list of YSO candidates associated with Perseus using the combined IRAC and MIPS data, which is beyond the scope of this paper. As part of the c2d ancillary data, there has been a paper on the Bolocam 1.1 mm continuum survey of Perseus (Enoch et al. 2006) and one on the James Clerk Maxwell Telescope (JCMT) SCUBA submillimeter maps from the COMPLETE team as compared to the *Spitzer* data (Jørgensen et al. 2007).

This paper can be broadly divided into three major parts. First, we give the details of the observations, reductions, and source

TABLE 1
SUMMARY OF OBSERVATIONS (PROGRAM 178)

FIELD	MAP CENTER		FIRST-EPOCH AOR Key	SECOND-EPOCH AOR Key
	R.A.	Decl.		
per1	03 47 05.0	+32 38 23.0	5780992	5787648
per2	03 44 30.7	+32 06 08.1	5781248	5787904
per3	03 42 34.5	+31 55 33.0	5781504	5788160
per4	03 40 39.0	+31 37 53.0	5781760	5788416
per5	03 37 42.0	+31 16 41.0	5782016	5788672
per6	03 33 34.0	+31 08 57.0	5782272	5788928
per7	03 31 10.6	+30 51 12.0	5782528	5789184
per8	03 29 10.0	+31 11 00.0	5782784	5789440
per9	03 30 54.0	+30 00 48.0	5783040	5789696
per10	03 28 26.0	+30 39 55.0	5783296	5789952
per11.............	03 26 11.0	+30 32 03.0	5798656	5790208

NOTE.—Units of right ascension are hours, minutes, and seconds, and units of declination are degrees, arcminutes, and arcseconds.

extraction (§ 2). This is followed by a presentation of the ensemble MIPS results for the entire Perseus cloud (§ 3). Finally, § 4 gives a focused discussion of noteworthy stellar aggregates and individual young stars. The main results of our study are summarized in § 5.

2. OBSERVATIONS, DATA REDUCTION, AND SOURCE EXTRACTION

2.1. *Observations*

The MIPS observations of Perseus were conducted on 2004 September 18–20 and covered ~ 10.5 deg^2; they were designed to cover the $A_V = 2$ contour, which then by extension completely covered the c2d IRAC map of Perseus. The center of this large map is roughly at $(\alpha, \delta) = (3^h 37^m, 31°11'30'')$ (J2000.0), or galactic coordinates $(l, b) = (160°, −19.5°)$, or ecliptic coordinates $(59.5°, +11.5°)$ (J2000.0).

These observations were part of *Spitzer* program ID 178; "AOR Keys" labeling the data sets in the *Spitzer* Archive are given in Table 1. Fast scan maps were obtained at two separate epochs. At each epoch, the spacing between adjacent scan legs was $240''$. The second-epoch observation was offset $125''$ in the cross scan direction from the first, to fill in the 70 μm sky coverage, which was incomplete at each individual epoch. Furthermore, the second-epoch scan was also offset $80''$ from the first along the scan direction, to maximize 160 μm map coverage in the combined epoch mosaic. These mapping parameters resulted in every part of the map being imaged at two epochs at 24 μm and only one epoch at 70 and 160 μm, with total integration times of 30, 15, and 3 s at each point in the map, respectively. The 160 μm maps have some coverage gaps and suffer from saturation (particularly in NGC 1333 and IC 348). Figure 1 shows the region of three-band coverage with MIPS and the four-band coverage with IRAC. At about 10.5 deg^2, the MIPS observations cover a much larger area than the IRAC observations, which cover only ~ 4 deg^2. The three main reasons for this apparent mismatch are entirely instrumental: (1) we are constrained by the ecliptic latitude to observe with scan legs in a particular orientation (the maximum rotation is about 10°), (2) we are limited in the available choices for scan leg lengths, and (3) MIPS covers large areas very efficiently, so we can easily cover large areas with MIPS in much less time than for IRAC.

The c2d MIPS observations were designed for even coverage (all to the same exposure time depth), independent of the
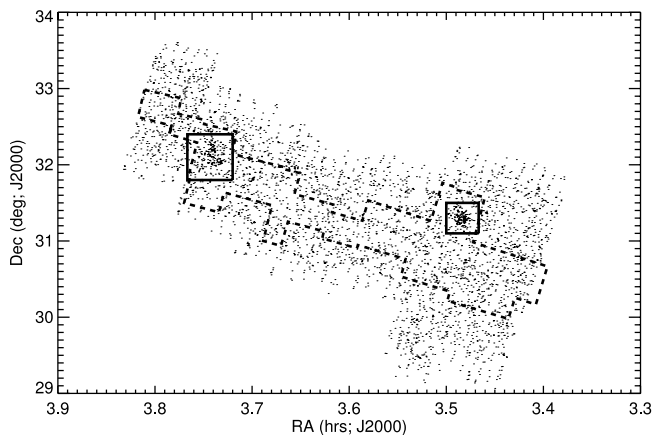
FIG. 1.—Location of MIPS coverage (small points are MIPS-24 detections), with the region of IRAC coverage (*dashed line*) indicated. The solid boxes indicate the regions defined to be IC 348 (*left*) and NGC 1333 (*right*). The definition of IC 348 includes the new objects recently found by Lada et al. (2006).

GTO observations of IC 348 (Lada et al. 2006) and NGC 1333 (R. Gutermuth et al. 2007, in preparation). The GTO observations of these regions are *not* included in the discussion here, primarily to enable discussion of a catalog obtained to uniform survey depth. This is different from the c2d IRAC observations of Perseus discussed in J06, where the GTO observations provided the images for one of the two epochs.

The two observation epochs were separated by 3–6 hr to permit asteroid removal in this relatively low ecliptic latitude ($+11°$–$12°$) field. Indeed, by comparing the 24 μm maps obtained at the two epochs, at least 100 asteroids are easily visible, ranging in flux density from at least as faint as 0.6 to as bright as 30 mJy. Some asteroids are clearly visible even at 70 μm. The asteroids in this and other c2d cloud maps will be discussed further in K. Stapelfeldt et al. (2007, in preparation).

We started with the *Spitzer* Science Center (SSC) pipeline-produced basic calibrated data (BCDs), version S11.4. For a description of the pipeline, see Gordon et al. (2005). As in Chapman et al. (2007), each MIPS channel was then processed differently and therefore is discussed separately below. Mosaics and source

catalogs from these data were delivered back to the SSC for distribution.[14] Multiple deliveries were made; the data discussed here were part of the 2005 data delivery.

Figures 2, 3, and 4 show the individual mosaics by channel, and Figure 5 shows a three-color image with all three channels included. (For an indication of where "famous" regions are, please see Fig. 16 below, which indicates several objects highlighted for discussion below.) There is substantial extended emission in all three MIPS channels throughout the MIPS maps. In the 70 and 160 μm channels, the MIPS instrument uses internal stimulator flashes to calibrate the data (for more information, see the *Spitzer* Observer's Manual, available at the SSC Web site[15]). For most of a scan leg, the correct calibration can be obtained via an interpolation. On the ends of scan legs, it necessarily must use extrapolation solutions. When the ends of the scan legs run across particularly bright emission, as they do in some cases here (particularly in the "ring" of bright emission), the absolute calibration is not as good as it is in darker regions. Fluxes obtained in these regions have larger errors than the rest of the map.

The IC 348 and NGC 1333 regions are encompassed by the overall Perseus cloud map data set. To explore the difference between the membership of these two clusters and the more broadly distributed Perseus young stellar population, we have chosen to consider the IC 348 and NGC 1333 stellar populations separately from the rest of the cloud (see Fig. 1). We have defined the regions belonging to the clusters based on the surface density of 24 μm sources. The region we define to be IC 348 is given by a box bounded by the coordinates $\alpha = 55.8°$–$56.5°$ (3.720^h–3.767^h, or $03^h43^m12.0^s$ to $03^h46^m00.0^s$), $\delta = 31.8°$–$32.4°$ (or $+31°48'00.0''$ to $+32°24'00.0''$). This region is larger than what has historically been assumed to encompass the cluster, and large enough (0.36 deg^2) to include the $\sim$300 likely cluster members (with the new likely members) found by Lada et al. (2006), but not so large that it includes substantial numbers of likely field members. (Note that this box includes most of the new members found by Cambresy et al. [2006] but does not include their farthest southwest part of the cluster.) The region we define to be NGC 1333
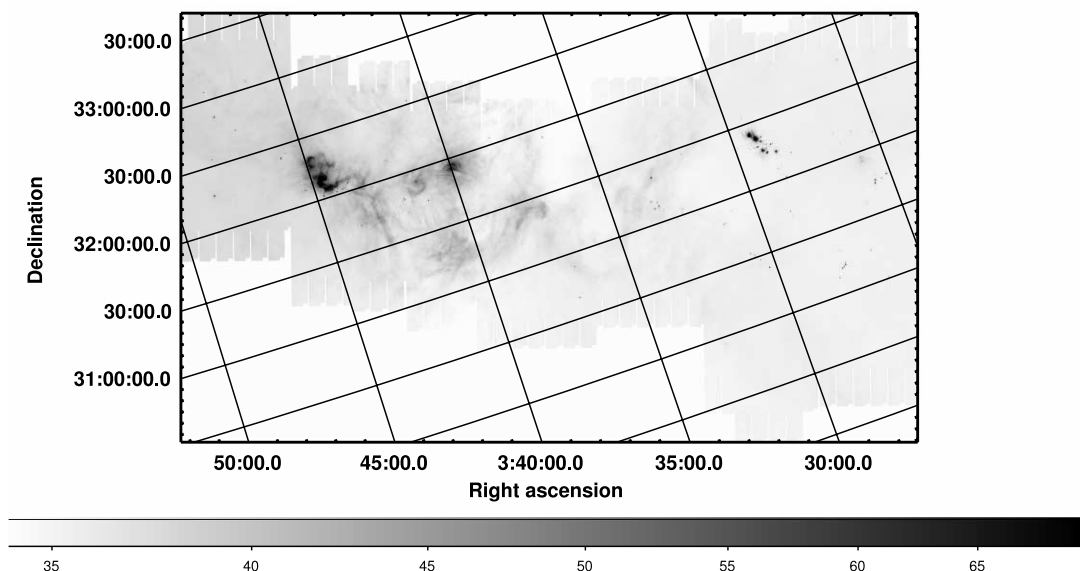
FIG. 2.—Mosaic of Perseus map at 24 μm. The reverse gray-scale colors correspond to a logarithmic stretch of surface brightnesses.
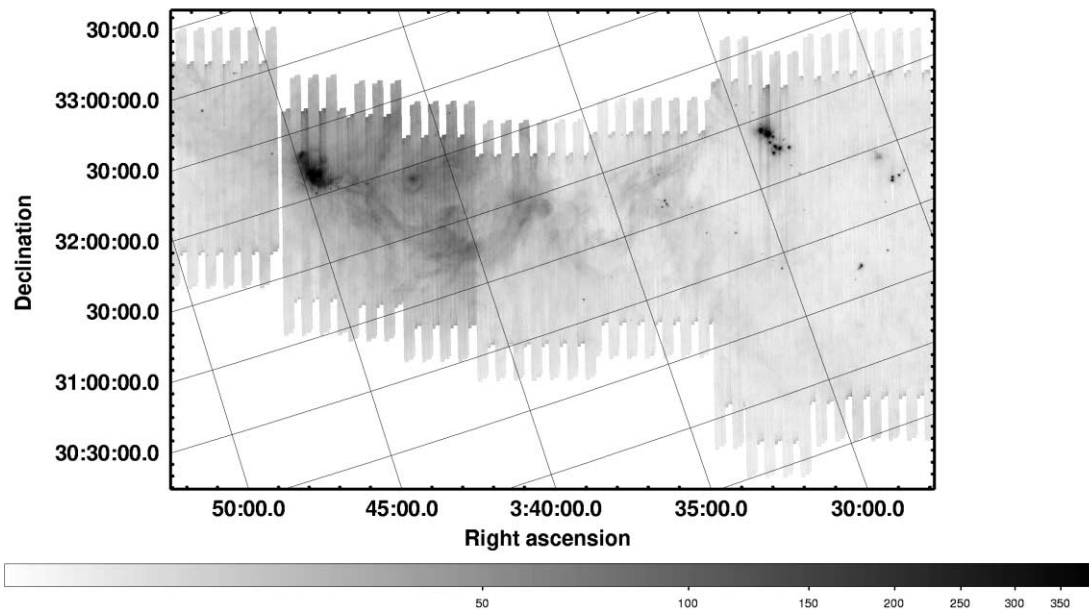
Fig. 3.—Mosaic of Perseus map at 70 μm. The reverse gray-scale colors correspond to a logarithmic stretch.

is given by a box bounded by the coordinates $\alpha = 52°$–$52.5°$ (3.467^h–3.500^h, or $03^h28^m00.0^s$ to $03^h30^m00.0^s$), $\delta = 31.1°$–$31.5°$ (or $+31°06'00.0''$ to $+31°30'00''$); this region is 0.17 deg^2. In both cases, for ease of comparison, these regions are the same as those used in J06.

2.2. MIPS-24

As discussed in Chapman et al. (2007), standard c2d pipeline processing on the S11 BCDs (2005 delivery) was used for MIPS-24 (Evans et al. 2005;[16] see also Young et al. 2005). In summary, the c2d reduction starts with the pipeline-produced BCDs and

then further processes them to remove artifacts, e.g., "jailbars" near bright sources. A mosaic was then constructed from the entire data set using the SSC MOPEX software (Makovoz & Marleau 2005; see also Fig. 2). Sources were extracted from the mosaic and band merged into the catalog along with Two Micron All Sky Survey (2MASS; Skrutskie et al. 2006) JHK_s and IRAC-1, IRAC-2, IRAC-3, and IRAC-4 measurements. For more details on this process, please see Chapman et al. (2007). The uncertainty on the flux densities derived at 24 μm is estimated to be 15%.

The high-quality catalog we assembled consisted of all detections at MIPS-24 from the last 2005 delivery where the c2d catalog detection quality flag (see the 2005 c2d Delivery Document[17])

---

[16] See http://data.spitzer.caltech.edu/popular/c2d/20050705_enhanced_v1/Documents/.
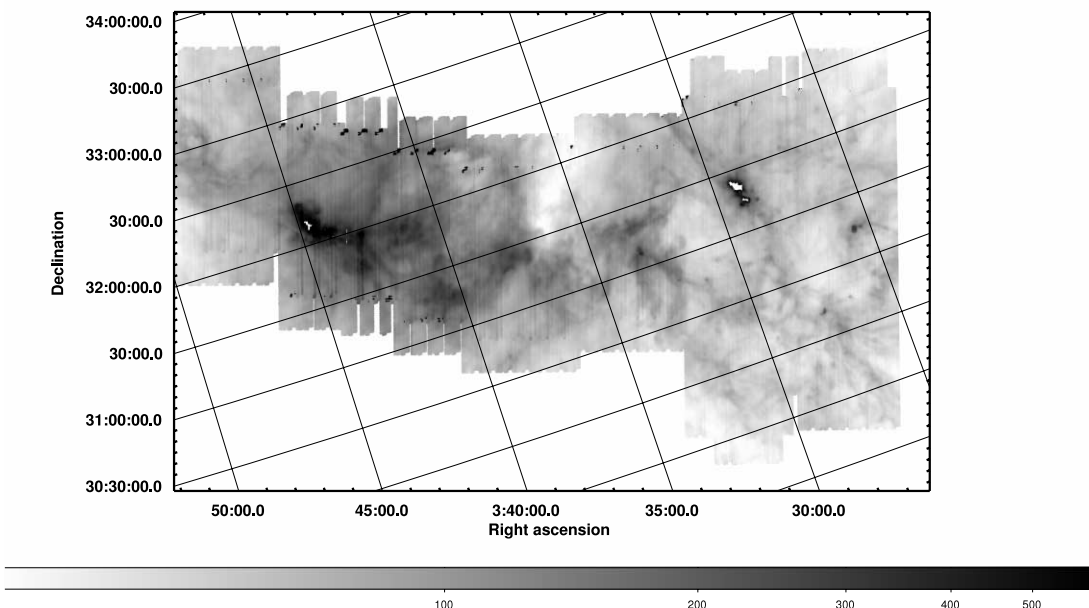
[17] Available at http://ssc.spitzer.caltech.edu/legacy/.

Fig. 4.—Mosaic of Perseus map at 160 μm. The reverse gray-scale colors correspond to a logarithmic stretch.
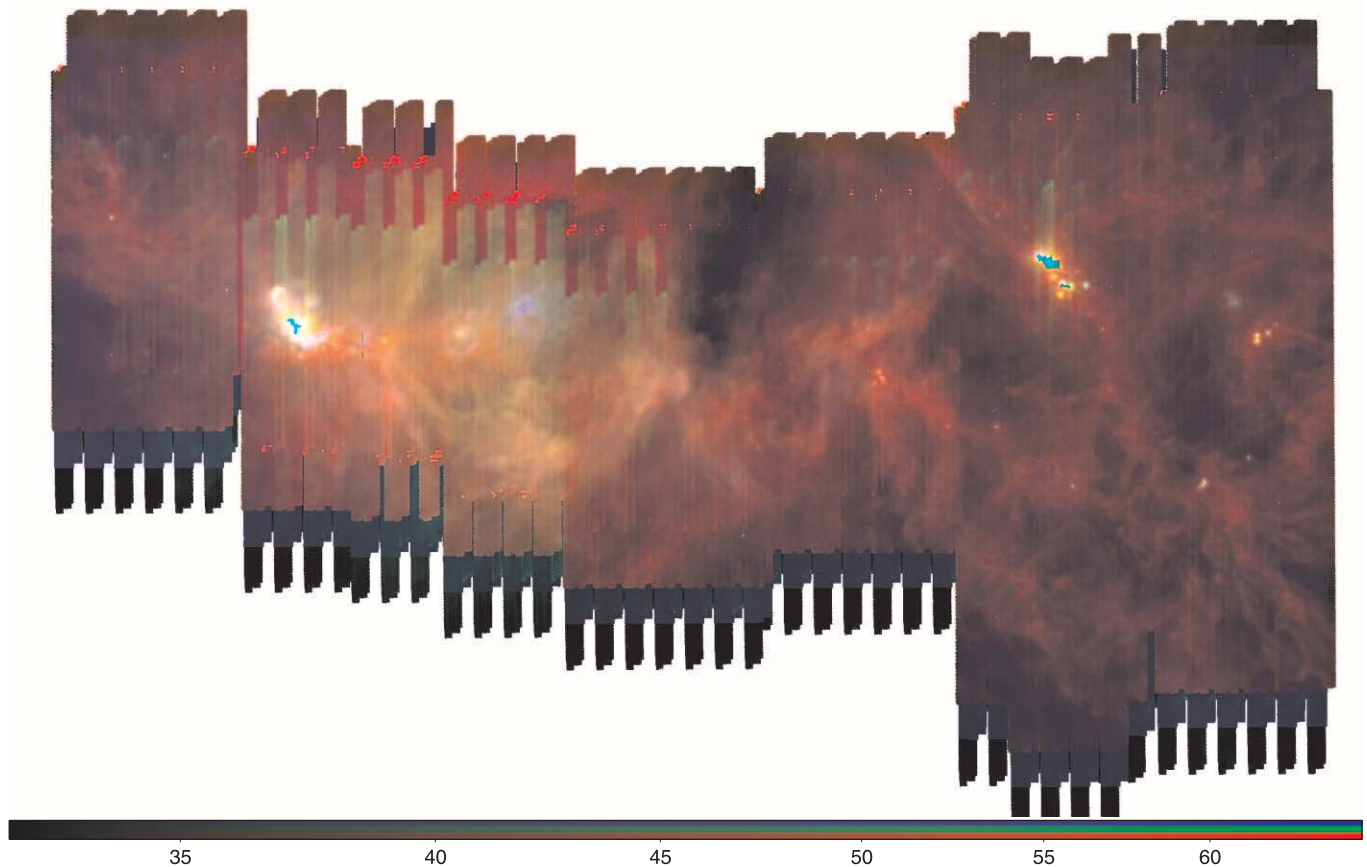
Fɪɢ. 5.—Three-color mosaic of Perseus map at 24 (*blue*), 70 (*green*), and 160 μm (*red*).

was "A" or "B," which translates to a signal-to-noise ratio of >5, and where the object was detected at both epochs. While resulting in a shallower survey than would be possible using other combinations of flags, this ensures that no asteroids are included in the catalog. The extraction pipeline flags some objects as extended ("imtype" flag); no filter was imposed on these extended objects to create the catalog we used, but only eight of the objects in our catalog are flagged as extended.

There were 3950 total point sources detected at 24 μm meeting our criteria, ranging from 0.603 to 3530 mJy (comparable to the saturation limit; see below). The source surface density is about 370 sources deg^{-2}. The zero point used to convert these flux densities to magnitudes was 7.14 Jy, based on the extrapolation from the Vega spectrum as published in the MIPS Data Handbook. About 30% of these objects had identifiable 2MASS counterparts at K_s.

The faint limit of the catalog of 24 μm sources is a function of the nebular brightness across the field, but what might be less obvious is that the saturation limit for point sources with MIPS-24 is also a function of location in the cloud because the total flux density registered by the detector is that due to the point source itself plus any surrounding extended nebular emission. Because the extended emission at 24 μm varies from $\sim$450 MJy sr^{-1} in IC 348 to $\sim$100 MJy sr^{-1} in NGC 1333 to $\lesssim$1 MJy sr^{-1} in the darker parts of the cloud, the completeness of the 24 μm catalog at both the bright and faint limits is a function of location in the cloud. For example, as will be seen in the source count discussion (§ 3.1), there are fewer faint sources in the clusters than in the field, and fewer bright sources in NGC 1333 than in IC 348. This may indeed be entirely due to the brightness of the background. An ad-

ditional issue when considering completeness is the resolution; the resolution of MIPS-24 ($\sim$6$''$, 2.55$''$ pixel size) is poorer than IRAC or 2MASS ($\sim$2$''$). Source multiplicity and confusion may also affect the completeness of the catalog, particularly in dense regions such as the clusters.

2.3. *MIPS-70*

To reduce the MIPS-70 data, we started with the automated pipeline-produced BCDs. The SSC produces two sets of BCDs; one is simply calibrated, and the other has spatial and temporal filters applied that attempt to remove instrumental signatures in an automated fashion. These filtered BCDs do not conserve flux for extended emission, nor for bright point sources, but they do conserve flux for the fainter point sources. We started with both the filtered and unfiltered S11 BCD products. Then, we mosaicked these individual BCDs into one filtered and one unfiltered mosaic using the MOPEX software. We resampled the pixels to be 4$''$ square (smaller than the native pixel scale of $\sim$10$''$) to better enable source extraction. The unfiltered mosaic is presented in Figure 3 to better show the extended emission.

We defined the point response function (PRF) from clean and bright point sources selected from this large mosaic and then, using this, performed point-source detection and extraction using the APEX-1 frame option of MOPEX. The initially produced source list was cleaned for instrumental artifacts via manual inspection of the 70 μm image and comparison to the 24 μm image; e.g., if there was some question as to whether a faint object seen at 70 μm was real or an instrumental artifact, and comparison to the 24 μm image revealed a 24 μm source, then the 70 μm object was retained as a real source. This catalog also has the

same limitations as was found at 24 μm; the brightness of the nebulosity drowns out the faintest objects in the clusters and contributes to saturation of the brightest point-source objects (particularly in the clusters) as well. In addition, the resolution at 70 μm ($\sim20''$) is coarser than it is at 24 μm ($\sim6''$), which complicates source matching to K_s and source extraction in confused regions such as the clusters. For all of these reasons, the 70 μm catalog is not necessarily complete and unbiased, particularly in the regions of bright ISM and/or the faintest end.

Based on a comparison of PRF and aperture photometry fluxes, we empirically determined the limit between where PRF fitting photometry on the filtered image was more appropriate (fainter than 4×10^3 mJy) and where aperture photometry with an aperture radius of $32''$ on the unfiltered image was more appropriate (brighter than this level). There were 19 objects brighter than 4×10^3 mJy, for which we used aperture photometry with a $32''$ aperture and a 17% aperture correction. The estimated uncertainty on our point-source fluxes is 20%. No color corrections were applied. Sources that were determined by APEX to be extended were not fitted, so sources that appear at initial manual inspection to be pointlike but are actually resolved in the 70 μm maps do not appear in our catalog.

There were 139 total point sources detected at 70 μm, ranging from 64 mJy[18] to 97 Jy;[19] the surface density is about 13 sources deg^{-2}. About 90% of the 70 μm objects had identifiable counterparts at 24 μm. The zero point used to convert the flux densities to magnitudes was 0.775 Jy, based on the extrapolation from the Vega spectrum as published in the MIPS Data Handbook.

2.4. MIPS-160

For the 160 μm data, we started with the S11.4 SSC BCDs. To create the mosaics that appear in the figures in this paper (such as Fig. 4), we used MOPEX to mosaic the unfiltered BCDs and resampled the mosaics to have $8''$ pixels (half the native pixel scale). In order to "fill in" the gaps in the map caused by incomplete coverage, we used a two-dimensional 3×3 (native) pixel boxcar median to interpolate across missing ("NaN") pixels. No attempt was made to interpolate across saturated regions, nor was any further filtering applied to remove instrumental signatures.

In order to obtain point-source flux densities, we started with the unfiltered 160 μm pipeline products and created mosaics with pixels of similar size to the native pixel scale. Photometry was then performed with APEX-1 frame PRF fitting on this mosaic. Because of the complexity of the extended emission in this channel, APEX can be confused. APEX's initial source list was cleaned by hand, and only flux densities from those point sources considered reliable were retained. Not all emission peaks seen on the mosaic were retained; as for 70 μm, only unresolved point sources are included. Similarly, saturated sources, or close multiples, or low signal-to-noise ratio sources, are not included. As with the other MIPS wavelengths, in regions of particularly bright ISM (at 160 μm, the ISM is bright enough that this restriction is no longer limited just to the clusters), point sources may be lost due to saturation or (at the faint end) to simply being drowned out by the

nebulosity. Finally, source confusion is a particularly difficult problem here, where the resolution is $\sim40''$.

There are 28 total point sources in our catalog detected at 160 μm (see Fig. 13 below), ranging from 0.67 to 18 Jy. About 60% of the 160 μm objects had identifiable counterparts at 24 and 70 μm; many of the 160 μm–only objects are lacking shorter wavelength counterparts because the shorter wavelengths are saturated. The zero point used to convert the flux densities to magnitudes was 0.159 Jy, based on the extrapolation from the Vega spectrum as published in the MIPS Data Handbook.

No color corrections were applied, nor was any attempt made to remove the contribution from the blue filter leak. As discussed in the *Spitzer* Observer's Manual and the MIPS Data Handbook (available on the SSC Web site), stars fainter than $J \sim 5.5$ mag will not produce a detectable leak signal above the confusion level. Of the 12 objects detected at both J and 160 μm, all of them have J fainter than 5.5. We conclude that the leak is not important for our objects. We estimate an overall 160 μm flux uncertainty of 20%.

2.5. Band-merged Source Catalogs and Statistics

A multiwavelength mosaic using MIPS data can be found in Figure 5. The extended emission is particularly dramatic and complex when compared across all of the MIPS wavelengths.

The c2d project mapped this cloud in IRAC as well; the IRAC map (see J06) covers less than half the area covered by MIPS (see Fig. 1), so there are large parts of the MIPS map that do not have IRAC coverage. The IRAC source extractions discussed in J06 were band merged with the MIPS sources (see Chapman et al. [2007] or Harvey et al. [2006] for much more discussion on this multiwavelength band-merging process), and these were included in our catalog.

Table 2 presents some statistics on the ensemble catalog spanning J band through 160 μm. Whereas only 37% of the MIPS-24 objects in the entire catalog have an IRAC match at some band, 92% of the MIPS-24 objects *in the region covered by IRAC* have a match in at least one IRAC band. There are near-infrared (NIR) JHK_s data covering this entire region from 2MASS, but 2MASS is relatively shallow; only 29% of the MIPS-24 sources have K_s band counterparts.

We wish to remind our readers of the discussion in § 2, namely, that due to bright nebulosity, particularly in the clusters, both the faintest sources and the brightest sources (due to saturation) may not be present in the catalog. For example, about half of the 70 μm objects that lack 24 μm counterparts and about half of the 160 μm objects lacking 70 and 24 μm counterparts are lacking those counterparts solely because the shorter wavelength counterpart is saturated.

The c2d IRAC study by J06 selected YSO candidates using a preliminary SED classification scheme that required a source to be detected in one or more IRAC photometric bands. Perseus YSO candidates ("YSOc") selected in this fashion were statistically described by J06 and are not reproduced here. A new result presented here for those objects discussed in J06 is that $\sim80\%$ have MIPS-24 counterparts, $\sim13\%$ have MIPS-70 counterparts, and $\sim2\%$ have MIPS-160 counterparts. In the region of Perseus not covered by IRAC, we are limited to using $K - [24]$ colors to select YSO candidates. Further discussion of the global properties of these candidates appears below. An upcoming paper by S.-P. Lai et al. (2007, in preparation) will synthesize data from IRAC, MIPS, and ground-based surveys and present a list of all YSO candidates in this cloud based on *Spitzer* data. A separate study by M. Enoch et al. (2007, in preparation) will include very cold *Spitzer* objects associated with millimeter emission. Jørgensen

---

[18] An A0 photosphere with a 70 μm flux density of this value would have $K_s \sim 2.9$ mag.

[19] Although the instrument's published saturation limits are about half of this value, some useful information can still be extracted from the first few reads of the BCDs. Note that the measured value of the flux of this bright object prior to the aperture correction is ~80 Jy. This value may not necessarily be well calibrated, as it is indeed quite bright.

TABLE 2
Statistics of MIPS Point-Source Detections

Item	Overall	IC 348	NGC 1333	Rest of Cloud	IRAC Coverage Region
24 μm..	3950	252	166	3532	1602
70 μm..	139	11	21	107	85
160 μm..	28	0	1	27	15
24 and 70 μm	121	9	13	99	85
24, 70, and 160 μm..............................	16	0	0	16	i 13
24 μm and 2MASS *K*	1141	146	78	917	557
24 μm and any IRAC band.........................	1476	205	146	1125	1476
70 μm and any IRAC band.........................	91	10	16	65	83
160 μm and any IRAC band.......................	19	0	1	19	15

et al. (2007) discuss a comparison between the JCMT SCUBA submillimeter and *Spitzer* data in Perseus.

Finally, in the present paper we give only a statistical picture of the cloud population compared to the extragalactic source backgrounds. As with the other c2d papers in this series, our comparison extragalactic source background consists of data from the *Spitzer* Wide-area Infrared Extragalactic Survey (SWIRE; Lonsdale et al. 2003), which were retrieved for the ELAIS N1 field[20] and processed through the same steps as for the molecular cloud data. For further discussion of these steps, see Harvey et al. (2007).

2.6. *Summary of Observations*

This paper presents 10.5 deg^2 of Perseus as observed with MIPS at 24 μm (∼6″ resolution), 70 μm (∼20″ resolution), and 160 μm (∼40″ resolution). It references band-merged complementary data obtained with IRAC (3.6, 4.5, 5.8, and 8 μm) and 2MASS (*JHK_s*) over this same region. There were 3950 point sources detected at 24 μm, 139 point sources at 70 μm, and 28 point sources at 160 μm. The sensitivity limits for all three bands are a function of location on the sky because the sky brightness changes substantially at all three bands; it is brightest in the clusters IC 348 and NGC 1333. The rest of the analysis of the ensemble of point sources in Perseus separates out the objects found in the clusters from the rest of the cloud and compares them (where possible) to similar observations of one of the SWIRE fields, expected to be populated entirely by galaxies.

3. GLOBAL RESULTS ACROSS THE PERSEUS CLOUD

3.1. *Source Counts*

MIPS sources in Perseus are a combination of cloud members, foreground/background stars in the galaxy, and the extragalactic background. Figure 6 shows the observed Perseus 24 μm differential source counts in comparison to observed source counts from the SWIRE ELAIS N1 extragalactic field and to the prediction for Galactic star counts in the *IRAS* 25 μm band from the Wainscoat et al. (1992) model provided by J. Carpenter (2001, private communication). In the IC 348 and NGC 1333 clusters, there is a clear excess of cloud member sources above both backgrounds, for flux densities >2–3 mJy. In IC 348, there is suggestion of an excess even at the 1 mJy level. In NGC 1333, the source counts turn over at higher flux densities, presumably due to reduced sensitivity caused by source crowding and bright extended emission. Across the much larger "rest of the cloud" region, an excess of on-cloud sources is seen only for flux densities >10 mJy;

---

[20] VizieR Online Data Catalog, II/255 (J. Surace et al., 2004).

below this level, the Perseus source counts follow the extragalactic background. Galactic star counts make only a minor contribution to the MIPS source counts in Perseus, in contrast to the four other clouds surveyed by c2d (Evans et al. 2003). This is a natural consequence of Perseus's location at $l = 160°$, $b = -20°$, whereas the four other clouds are located toward the inner galaxy and closer to the Galactic plane.

Figure 7 shows 70 μm source counts in Perseus, along with extragalactic background counts from the SWIRE ELAIS N1 field. In the extended cloud outside the clusters, a clear excess in source counts is present above a flux density of 200 mJy. A similar result is found in IC 348. In NGC 1333, however, the flux density limit above which cluster number counts exceed the extragalactic background is about 65 mJy. The brightest measurable objects in Perseus are found in NGC 1333, where there is a clear excess of these relative to other parts of Perseus. It should be noted (see discussion in § 2.3) that the brightest sources (flux densities >20 Jy) are underrepresented in these plots due to saturation effects, that the faintest sources are both subject to the completion limitations discussed above and more difficult to detect in regions of high surface brightness, and that only point sources are included.

3.2. *Recovery of IRAS Sources*

The MIPS data for the Perseus molecular cloud offer an opportunity to assess how successful the *IRAS* survey was in identifying point sources in a complex region. We now explicitly compare the *IRAS* PSC (Beichman et al. 1988) and *IRAS* FSC (Moshir et al. 1992) results in this region to the *Spitzer* c2d images and catalogs described in this paper. Complex extended emission is present in all three MIPS bands, posing a significant source of confusion to the large *IRAS* aperture measurements. Many of the *IRAS* PSC objects were detected at 60 or 100 μm only, with only upper limits at 12 and 25 μm; so even without *Spitzer* data, one might suspect that such sources might correspond to texture in the extended emission. As we show below, the *Spitzer* data comparison clearly shows that significantly fewer spurious sources appear in the FSC than in the PSC.

The statistics are presented in Table 3. An *IRAS* data quality flag of 3 means a solid detection, whereas data quality flags of 1 indicate upper limits. "Cleanly retrieved" means that *IRAS* reported a single source at a given location, and the corresponding MIPS image shows a single object that in several cases was saturated. "Completely missing" means that no source appears at that location in the corresponding MIPS image, and there is no immediately apparent reason for the discrepancy. In contrast, "confused by nebulosity" means that the corresponding MIPS image shows structured nebulosity that could be confused for a point
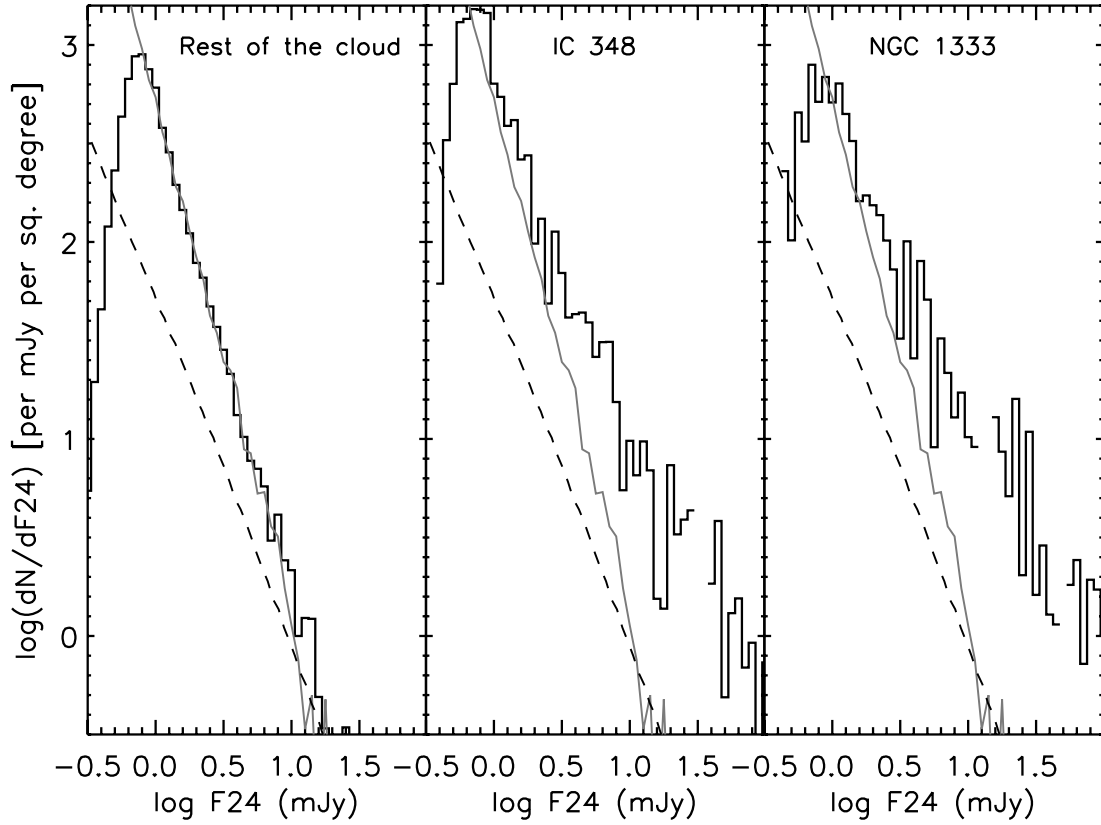
FIG. 6.—Differential number counts at 24 μm in Perseus. Extragalactic background source counts from the 6.1 deg^2 SWIRE ELAIS N1 field are shown for comparison (*thin solid line*), as well as predicted background star counts from the models of Wainscoat et al. (1992; *dashed line*). There is a clear excess of sources in the clusters that are likely cluster members. In the rest of the cloud, an excess of on-cloud sources is seen only for flux densities >10 mJy; below this level, the Perseus source counts follow the extragalactic background.
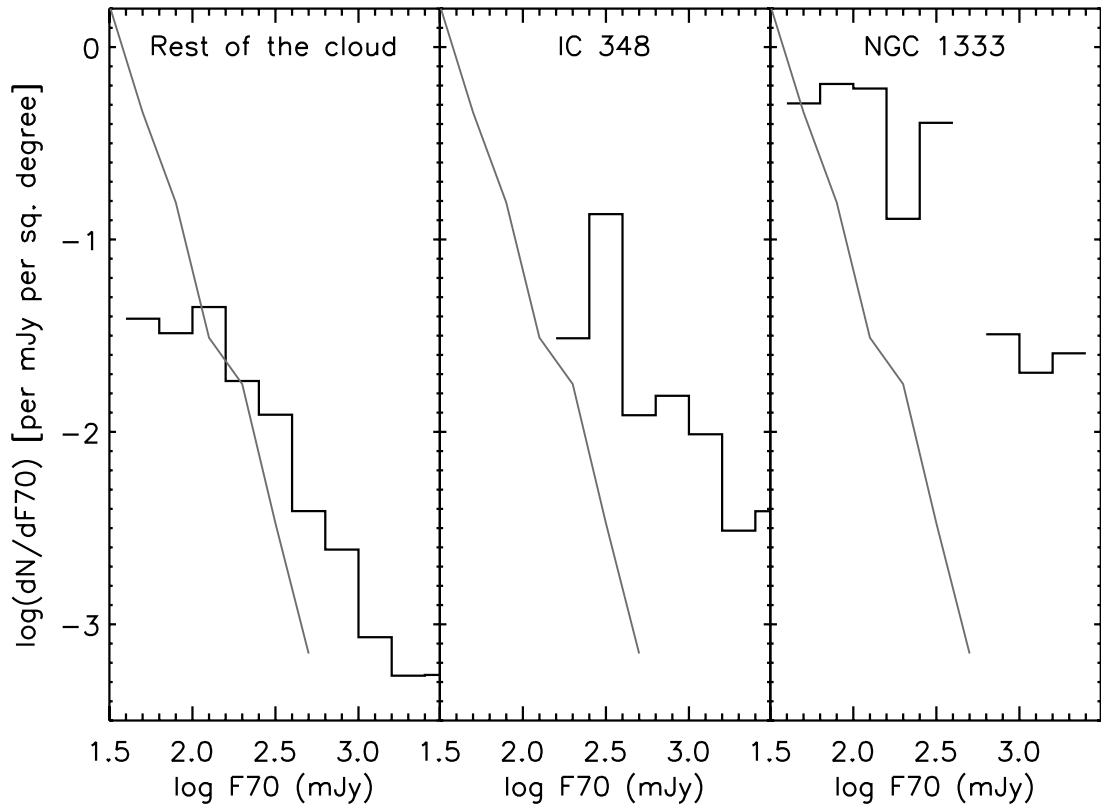

FIG. 7.—Differential number counts at 70 μm in Perseus. Extragalactic background source counts from the 6.1 deg^2 SWIRE ELAIS N1 field are shown for comparison (*thin solid line*). There is a clear excess of Perseus cloud sources above the extragalactic background, for flux densities >200 mJy, in all three regions.

TABLE 3
IRAS Results in MIPS Perseus Map Region

Item	At 24 μm	At 70 μm
12 μm PSC real (*IRAS* qual = 3) detections	51	51
Cleanly retrieved...	34 (67%)	19 (37%)
Completely missing	1 (2%)	16 (31%)
Confused by nebulosity	11 (21%)	15 (29%)
Resolved as multiple...	5 (10%)	1 (2%)
25 μm PSC real (*IRAS* qual = 3) detections	56	56
Cleanly retrieved...	34 (61%)	31 (55%)
Completely missing	0 (0%)	6 (11%)
Confused by nebulosity	13 (23%)	17 (30%)
Resolved as multiple...	9 (16%)	2 (4%)
60 μm PSC real (*IRAS* qual = 3) detections	88	80
Cleanly retrieved...	32 (36%)	35 (44%)
Completely missing	9 (10%)	8 (10%)
Confused by nebulosity	42 (48%)	36 (45%)
Resolved as multiple...	5 (6%)	1 (1%)
100 μm PSC real (*IRAS* qual = 3) detections	78	75
Cleanly retrieved...	10 (13%)	9 (12%)
Completely missing	41 (52%)	40 (53%)
Confused by nebulosity	25 (32%)	25 (33%)
Resolved as multiple...	2 (3%)	1 (1%)
12 μm FSC real (*IRAS* qual = 3) detections	56	57
Cleanly retrieved...	48 (86%)	24 (42%)
Completely missing	4 (7%)	27 (47%)
Confused by nebulosity	2 (3.5%)	5 (9%)
Resolved as multiple...	2 (3.5%)	1 (1%)
25 μm FSC real (*IRAS* qual = 3) detections	52	50
Cleanly retrieved...	38 (73%)	26 (52%)
Completely missing	1 (2%)	10 (20%)
Confused by nebulosity	8 (15%)	11 (22%)
Resolved as multiple...	5 (10%)	3 (6%)
60 μm FSC real (*IRAS* qual = 3) detections	0	0
100 μm FSC real (*IRAS* qual = 3) detections	0	0

source in the large *IRAS* beams. Finally, "resolved as multiple" means that MIPS finds multiple far-infrared sources where *IRAS* reported only one.

As can be seen in Table 3, most of the 12 and 25 μm highest quality PSC point sources are retrieved, or it is clear why a point source was reported for that location. Overall, 20%–30% of the "point sources" at 12 and 25 μm resolve into knots of nebulosity. Essentially none of these 12 and 25 μm point sources are undetected at 24 μm, but a much larger fraction are completely missing at 70 μm: this is likely to be a result of the lower sensitivity of 70 μm compared to 24 μm combined with the lower expected flux density from stars at 70 μm compared with the shorter wavelengths.

There are many more "point sources" reported at 60 and 100 μm (than at 12 and 25 μm) in the PSC. A much lower fraction of these objects are recovered; many more of these are completely missing or fall apart into nebulosity when viewed with MIPS. More than half of the 100 μm point sources are completely missing, and 25%–40% of the 100 and 60 μm point sources are clearly confused by nebulosity.

Surprisingly few *IRAS* sources are resolved into multiple objects by *Spitzer*. However, our results may be a lower limit on the true number of such objects, as we did not consider the individual error ellipses for each *IRAS* source. Two *IRAS* sources clearly resolved into stellar aggregates are discussed below in §§ 4.1.2 and 4.1.3.

Overall, a much larger fraction of FSC objects are recovered by MIPS than PSC objects. This is largely due to the FSC being

far more cautious about claiming to detect point sources in the presence of cirrus confusion: no 60 or 100 μm detections are listed in this region in the FSC, whereas the PSC lists numerous detections that appear to be spurious. At 12 and 25 μm, unrecognized asteroids may be responsible for the lower recovery rate of PSC sources relative to the FSC. We conclude that the *IRAS* FSC is much more robust for studies of stellar sources in regions with complex extended emission and should be used in preference to the *IRAS* PSC unless *Spitzer* MIPS data are available. A list of high-quality *IRAS* detections that are missing or fall apart into nebulosity in our Perseus MIPS data set appears in the Appendix.

We note for completeness that direct comparison of the measured MIPS and *IRAS* flux densities for the same sources is greatly complicated by the different calibration approaches of the two instruments, requiring detailed knowledge of the underlying SED of the objects in question and large color corrections. This is beyond the scope of this paper.

3.3. *Color-Magnitude and Color-Color Plots*

3.3.1. *The K_s versus $K_s - [24]$ Diagram*

Figure 8 shows the K_s versus $K_s - [24]$ color-magnitude diagram (CMD) for Perseus, combining our results with 2MASS survey data. Ordinary stellar photospheres (likely foreground or background stars) have $K_s - [24] \sim 0$. The lack of sources in the lower left of the K_s versus $K_s - [24]$ plot is entirely a sensitivity effect, explained as follows. Our K_s magnitudes are limited to those found in 2MASS, e.g., to brighter than $\sim$16th magnitude in this region. Our 24 μm survey goes down to about 1 mJy (see Fig. 6), which, for a stellar photosphere, corresponds to about $K_s \sim 10$, so we do not see any stellar photospheres with K_s fainter than $\sim$10. As we move to redder objects, source matches to fainter K_s are obtainable down to the 2MASS sensitivity limit. Background galaxies become numerous at $K_s > 14$.

The top left panel of Figure 8 shows data from the SWIRE extragalactic survey, as discussed above, which have been flux trimmed to match the c2d survey sensitivity. Since all of the objects in SWIRE are likely foreground stars or background galaxies, this panel shows which regions of the CMD are least likely to provide a clean sample of likely YSOs: objects with $K_s - [24] > 2$ and $K_s < 14$ are least likely to be part of the Galactic or extragalactic backgrounds, and thus likely to be YSOs with a 24 μm excess. There are many such stars with $K_s - [24]$ excesses in the rest of the cloud despite some expectations that there would be little star formation outside of the canonical clusters. Looking at the IC 348 and NGC 1333 clusters, there are comparatively not many stars or background galaxies; most of the objects are likely young cluster members.

There remains a possibility that some of the objects seen at 24 μm and having a $K_s - [24]$ color suggestive of disks may be background asymptotic giant branch (AGB) stars. Harvey et al. (2006, 2007) find that any AGB star in our Galaxy is likely to be saturated in the c2d IRAC observations, but the MIPS survey effectively reaches a different depth. The galactic coordinates of Perseus are $(160°, -19.5°)$, toward the Galactic anticenter and a significant angle out of the plane; the expected background star counts are relatively small. Assuming as a worst-case scenario that the Milky Way disk is 15 kpc radius and 1.5 kpc thick, the farthest reaches of our Galaxy that could be included in these observations of Perseus are $\sim$1–4 kpc away. We compared Figure 8 with data from Blum et al. (2006) obtained in the LMC. Assuming that the LMC is at 44 kpc, and correcting for the relative distances along the line of sight to Perseus, a typical AGB star would appear so bright as to be saturated in 2MASS. Only 0.06% of the
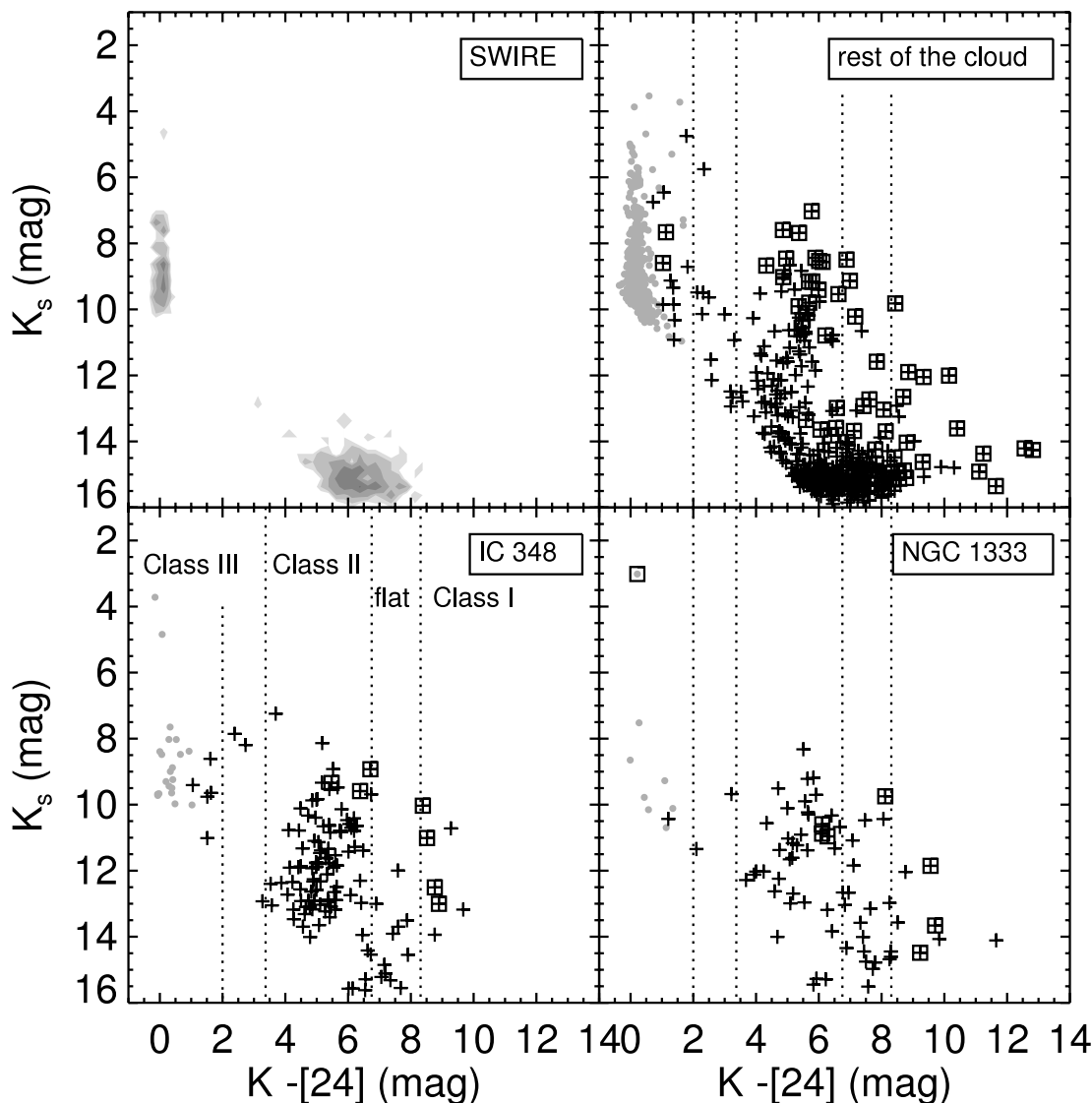
Fig. 8.—K_s vs. $K_s - [24]$ for objects in SWIRE (*contour plot, top left*), the rest of the cloud (*top right*), IC 348 (*bottom left*), and NGC 1333 (*bottom right*). Objects in SWIRE are expected to be mostly galaxies (objects with $K_s \gtrsim 14$) or stellar photospheres (objects with $K_s - [24] \lesssim 1$). For the remaining plots, filled gray circles are objects with SEDs resembling photospheres, and plus signs are the remaining objects. An additional box around a point denotes that it was also detected in 70 μm. Objects that are candidate young objects have colors unlike those objects found in SWIRE, e.g., $K_s \lesssim 14$ and $K_s - [24] \gtrsim 1$. Dashed lines denote the divisions between Class I, flat-spectrum, Class II, and Class III objects; to omit foreground and background stars, we have further imposed a $K_s - [24] > 2$ requirement on our Class III objects (see text). Based on the fraction of stars in the various classes, NGC 1333 is younger than IC 348; there are substantial numbers of young stars in the rest of the cloud.

distance-adjusted LMC sample would be unsaturated and appear in Figure 8, equivalent to just one of the 1141 2MASS sources within the Perseus map area. Larger AGB counts would be expected if the background population was highly reddened, but this is unlikely given that only 2% of the MIPS map area lies above the $A_v = 10$ contour. We therefore conclude that the vast majority of 297 objects with $K_s - [24] > 2$ and $K_s < 14$ are likely to be young stars associated with the Perseus clouds.

As a simple first attempt at classifying the objects found throughout our map into Class I, flat, Class II, and Class III objects, we can use the observed $K_s - [24]$ colors and assign an α index following Greene et al. (1994), where $K_s - [24]$ values >8.31 are Class I objects, those between 6.75 and 8.31 are flat-spectrum objects, those between 3.37 and 6.75 are Class II objects, and those with <3.37 are Class III. Note that the formal Greene et al. (1994) classification puts no lower limit on the colors of Class III objects (thereby including those with SEDs resembling bare stellar photospheres, and allowing for other criteria to define youth). In our

case, since we know little about many of these new objects, we have minimized the contamination from foreground/background stars by requiring $K_s - [24] > 2$ and limited the contamination from background galaxies by requiring $K_s < 14$. Note that there are likely to be true Perseus members that are excluded by these (conservative) criteria, but identifying them is beyond the scope of this paper. The number of reported Class III objects we derive is certainly a lower limit to the true values. Table 4 summarizes the numbers of the objects that meet these criteria found in each region. Comparable fractions (~7%) in both of the clusters and the rest of the cloud have colors consistent with Class I objects. A much larger fraction of objects in NGC 1333 (21%) than IC 348 (only 4%) have colors consistent with the "flat" classification, while only 8% of the sources in the rest of the cloud have flat SEDs. Our results for the frequency of Class I and flat-spectrum SEDs differ from those of J06, who report that 47% of the Perseus YSO population outside the two clusters falls into these SED categories. The different results can be traced to how YSO candidates

TABLE 4

CLASSIFICATION BASED ON THE K_s VERSUS $K_s - [24]$ DIAGRAM

Item	Rest of Cloud	IC 348	NGC 1333
Number of objects with K_s and 24 μm...	917	146	78
Number with $K_s - [24] > 2$, $K_s < 14$..	138	107	52
Number with $K_s - [24] > 2$, $K_s < 14$, and Class I $K_s - [24]$ color	9 (6%)	7 (6%)	4 (7%)
Number with $K_s - [24] > 2$, $K_s < 14$, and "flat" $K_s - [24]$ color....................	12 (8%)	5 (4%)	11 (21%)
Number with $K_s - [24] > 2$, $K_s < 14$, and Class II $K_s - [24]$ color................	105 (76%)	92 (85%)	35 (67%)
Number with $K_s - [24] > 2$, $K_s < 14$, and Class III $K_s - [24]$ color................	12 (8%)	3 (2%)	2 (3%)

are selected. The MIPS rest of cloud area covers ~ 10 deg^2, whereas the IRAC rest of cloud area of J06 is a factor of 3 smaller and covers a region of higher extinction. The ~ 140 MIPS YSO candidates outside the clusters are selected from their position in the K_s versus $K_s - [24]$ diagram, implicitly limiting this selection to objects bright enough to be detected at K_s in 2MASS; J06 considers 144 YSO candidates selected using the 2005 c2d SED classification scheme combining IRAC and MIPS measurements, with no flux cutoff. The J06 results therefore extend to less luminous YSOs than we have considered here.

The MIPS data show that the abundance of *bright* Class I and flat-spectrum sources is not higher in the rest of the cloud versus the NGC 1333 and IC 348 clusters. The results of J06 suggest that *faint* objects of these types are more abundant in the intercluster region of Perseus.

Just from Figure 8, it can be seen that there are many more Class II objects in IC 348 than in NGC 1333; 85% of the candidate young objects have colors consistent with Class II objects in IC 348, whereas 67% of the objects in NGC 1333 have similar Class II colors. These numbers suggest that NGC 1333 is younger than IC 348, consistent with expectations that IC 348 should be 1–2 Myr (e.g., Lada et al. 2006 and references therein) and NGC 1333 should be younger at <1 Myr (e.g., Wilking et al. 2004 and references therein). From Figure 8, in the rest of the cloud, there are many more stars and background galaxies than in the clusters. Somewhat surprisingly, as was found in J06, there are many YSO candidates in the rest of the cloud as well; in sheer numbers, there are as many candidate young objects outside the clusters as in the clusters. Using the relative fractions of "flat" and Class II object colors as a proxy for age, objects in the rest of the cloud are intermediate in age, on average, between IC 348 and NGC 1333. However, there is also a larger fraction of Class III objects in the rest of the cloud (8%) than there is in either of the clusters (2%–3%). These Class III objects are located essentially randomly across the cloud.

Of course, for much of this region, we have more information than just K_s and 24 μm measurements, and a more sophisticated classification scheme can be implemented. In the clusters, because these regions have IRAC coverage, essentially all of the YSO candidates have already been identified and classified (using the 2005 c2d classification scheme as described there) as part of J06; additional discussion will be provided by S.-P. Lai et al. (2007, in preparation). In the rest of the cloud, there are vast regions without four-band IRAC data; these include 36 objects with $K_s - [24]$ excesses (e.g., with $K_s < 14$ and $K_s - [24] > 2$) that are additional YSO candidates. A few of these are found near the ends of MIPS scan legs where their photometry is less reliable and thus could be spurious. But most are likely to be true cloud members, especially those clustered near L1448 on the far northwest side of the MIPS mosaic. Figure 9 shows where all ~ 300 sources with $K_s - [24]$ excesses are located in our mosaic.

Most of these are projected against the regions of highest extinction covered by the IRAC data of J06.

The objects in Figure 8 that also have 70 μm detections are generally the brightest objects. This is effectively an instrumental artifact in the following sense. The intrinsic instrumental point-source sensitivity is worse at 70 μm than at 24 μm; for our observing strategy, the expected 1 σ point-source sensitivity is 0.25 mJy at 24 μm and 14.5 mJy at 70 μm. The faintest object we actually see in this cloud at 24 μm is 100 times fainter than the faintest object seen at 70 μm. Based on very simple SEDs, we expect that Class 0 objects through Class III objects could have a 24 μm : 70 μm flux ratio of ~ 10 to ~ 0.1. Thus, only the brightest cloud member objects will be detected at 70 μm as well as 24 μm. Conversely, most of the objects detected at 70 μm are bright enough that they are likely cloud members. There are three objects detected at 70 μm with $K_s - [24] < 3$ whose SEDs through 24 μm resemble photospheres. They are SSTc2d 032740.5+311539 (also known as VSS IX-12; Vrba et al. 1976), SSTc2d 032807.6+311040 (also known as VSS IX-11 and IRAS 03250+3100), and SSTc2d 032820.9+294757 (also known as SAO 75942). VSS IX-11 is in NGC 1333 (a portion with only two-band IRAC coverage), and it appears to retain a stellar (Rayleigh-Jeans) slope through 70 μm. The other two objects (VSS IX-12 and SAO 75942) are from outside the clusters, in regions with no IRAC coverage, and they both appear to have a clear excess at 70 μm, suggesting Class II SEDs. VSS IX-12 is extremely faint at 70 μm; SAO 75942 is a clear detection. Additional follow-up observations
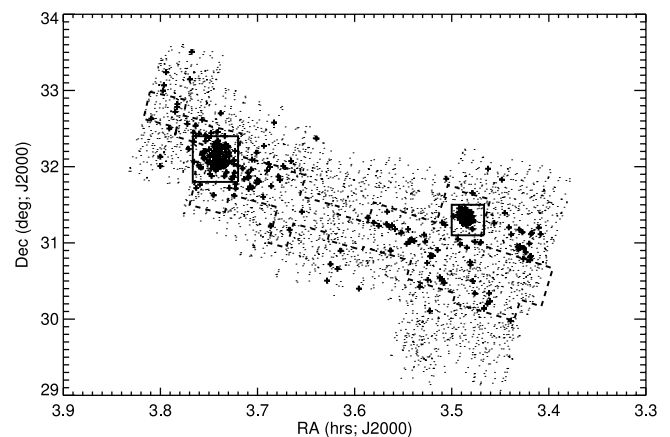

FIG. 9.—Locations of all objects detected at MIPS-24 (*small dots*) and the MIPS YSO candidates (*plus signs*), as defined by $K_s - [24] > 2$ and $K_s < 14$. The dashed line denotes the region of $A_V > 3$ covered in the *Spitzer* IRAC images of J06. Solid boxes outline the regions defined for the IC 348 and NGC 1333 clusters, as in Fig. 1. There are 36 objects with excesses outside the high-extinction region. Some of these are located near the ends of scan legs comprising the mosaics, so their photometry is less reliable. A few may be background galaxies. Some are likely to be more distributed cloud members, especially those clustered just north of L1448 on the western side of the mosaic.

TABLE 5
Very Red Objects Selected by a Variety of Means

SSTc2d Name	$K_s - [24]$[a]	$K_s - [70]$[b]	$[24] - [70]$[c]	Missed Match[d]	Other Name	Notes
032637.4+301528	Yes	Yes	...	...	IRAS 03235+3004	See § 4.2 and J06
032800.4+300801	Yes	...	...	...	IRAS 03249+2957	See J06
033015.1+302349	Yes	Yes	...	...	IRAS 03271+3013	See § 4.1.1
034202.1+314801	Yes	...	...	...	...	See § 4.1.2
032845.3+310541	Yes	Yes	...	...	HH 340	See § 4.2
033925.5+321707	Yes	...	...	...	...	See § 4.2
032839.6+311731	Yes	...	...	...	LAL 68	In NGC 1333
032858.4+312217	Yes	...	...	...	LAL 166	In NGC 1333
032903.3+312314	Yes	...	...	...	LAL 191	In NGC 1333
032912.9+311814	Yes	...	...	...	ASR 30	In NGC 1333
033309.5+310531	Yes	...	...	...	...	In B1 region
033316.6+310755	Yes	Yes	...	...	IRAS 03301+3057	In B1 region; see J06
033925.5+321707	...	Yes	...	...	IRAS 03363+3207	See § 4.2
032548.2+305537	...	Yes	...	Yes, but extended at 24 μm	BD +30 540	See § 4.5
032904.2+311608	...	Yes	...	Yes, but saturated 24 μm	...	In NGC 1333; see § 3.3.2
033554.4+304500	...	Yes	...	...	2MASS 03355439+3045011	See § 3.3.2
034443.9+320136	...	Yes	...	...	IRAS 03415+3152	On edge of IC 348; see § 3.3.2
032910.5+311330	...	...	Yes	...	IRAS 4 A1/A2	In NGC 1333
033121.0+304530	...	...	Yes	...	IRAS 03282+3035	See J06
033316.5+310652	...	...	Yes	...	B1-d	See J06
033218.0+304946	...	...	Yes	...	IRAS 03292+3039	See § 4.2 and J06
034356.9+320304	...	...	Yes	...	IC 348 MMS	See § 4.6
034741.6+325143	...	...	...	Yes, no 24	B5 IRS 1	See J06
032851.6+304502	...	...	...	Yes, no 24	LkHα 325	See § 3.3.4
033227.5+310236	...	...	...	Yes, no 24, 70	...	In B1 region, shorter saturated
033310.3+312108	...	...	...	Yes, no 24, 70	...	In B1 region, shorter saturated
033327.0+310647	...	...	...	Yes, no 24, 70	...	In B1 region, shorter saturated
032842.8+311744	...	...	...	Yes, no 24, 70	...	Shorter saturated
034107.8+314411	...	...	...	Yes, no 24, 70	...	Shorter saturated
033511.5+312026	...	...	...	Yes, no 24, 70	...	Very weak at 160, real?
032923.9+313320	...	...	...	Yes, no 24, 70	...	Diffuse at 160, offset from nearby bright object
033046.4+303242	...	...	...	Yes, no 24, 70	...	Diffuse at 160, offset from nearby bright object

[a] Objects where $K_s - [24] > 9.7$ mag.
[b] Objects where $K_s - [70] > 15$ mag.
[c] Objects where $[24] - [70] > 7$ mag.
[d] Objects that were detected at 70 without a 24 counterpart, or detected at 160 without 24 or 70 counterparts.

(such as MIR spectroscopy) will be needed to determine if these are true debris disk objects.

Low-luminosity cloud members are particularly interesting objects for study. Unfortunately, the SWIRE observations show that there is a large population of red background galaxies at $K_s > 14$, and so it is not generally possible to distinguish faint YSOs from background galaxies using broadband photometry alone. An important exception is the case of the reddest sources; at $K_s - [24] > 9.7$, there are no background galaxies with 2MASS counterparts. There are 12 such objects in Perseus (see Table 5); these are potentially the most embedded and therefore youngest cloud members. Four are located in NGC 1333, and two more are in the B1 region. IRAS 03301+3057 is one of the reddest objects in the entire cloud, turning up as red by using more than one criterion (see Table 5).

3.3.2. The K_s versus $K_s - [70]$ Diagram

Figure 10 shows the K_s versus $K_s - [70]$ CMD for Perseus, with data for the full SWIRE survey included for comparison. The morphology of this parameter space is similar to that of Figure 8 in that the survey sensitivity limits create the absence of points in the lower left, stellar photospheres are in the upper left (only one very bright Perseus object, in NGC 1333, appears in this region), and likely galaxies are fainter in K_s. There are roughly two clumps of objects in Perseus; the fainter clump is reasonably well matched in color and K_s to the objects found in SWIRE. There are very few such candidate galaxies in the two clusters because the bright ISM cuts off the sensitivity at a shallower level than elsewhere in the cloud. The SWIRE survey, because it is deeper than the c2d surveys, has objects that extend bluer in $K_s - [70]$ at the faintest K_s values than are found in Perseus. However, the reddest objects in SWIRE at these K_s magnitude levels are $K_s - [70] \sim 14$, all with $K_s > 13$. The reddest objects (redder than $K_s - [70] \sim 14$) are therefore likely to be Perseus cloud members and correspond to the most highly embedded objects. Most of these very red objects are distributed outside the two clusters, with only one in IC 348.

The brighter clump of objects (with $K_s \sim 10$) are also likely YSO candidates, and there are such candidates in all three Perseus regions; there is even one in SWIRE, suggesting that perhaps not all of the brighter objects are guaranteed to be YSOs. There is just one very bright object at 70 μm that is a likely stellar photosphere: it is SSTc2d 032807.6+311040 (also known as VSS IX-11 and IRAS 03250+3100), in NGC 1333. There is only one photosphere because of the shallow limits of our survey; this object, as bright as it is in K_s, is near our detection limit in 70 μm. There are not many
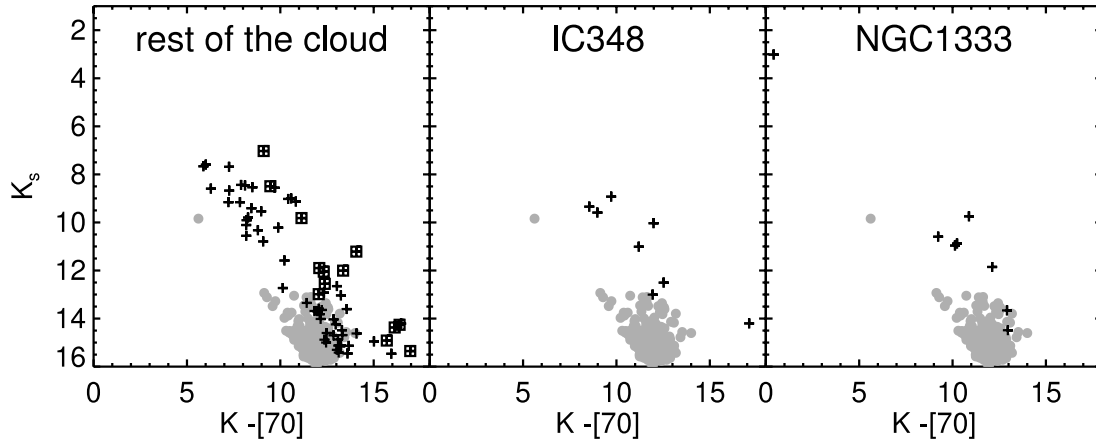
Fig. 10.—K_s vs. $K_s - [70]$ CMD for Perseus (*plus signs*), with data for the full SWIRE survey (*filled gray circles*) included for comparison. An additional box around an object denotes that it was also detected at 160 μm. The fainter clump of objects near $K_s \sim 15$ is extragalactic, and the brighter clump ($K_s < 12$) is YSO candidates. The reddest objects in SWIRE are $K_s - [70] \sim 14$, all with $K_s > 13$. In Perseus, objects redder than $K_s - [70] \sim 14$ are the most embedded objects; there are several such candidates for very embedded objects in the rest of the cloud, and one in IC 348. There are YSO candidates in all three Perseus regions. There is one very bright object at 70 μm in Perseus that is a likely a stellar photosphere: it is in NGC 1333, near $K_s \sim 3$ and $K_s - [70] \sim 0$.

objects in Perseus that are bare photospheres and also bright enough at 70 μm to be detected by our survey.

We attempted to compare these observed colors with *IRAS* measurements of two famous well-known young objects in Taurus from Kenyon & Hartmann (1995), even though the *IRAS* and MIPS bandpasses are not well matched. DO Tau is a classical T Tauri star (CTTS) with a $K - [60]$ color of 9.4 mag, and IRAS 04016+2610 is a more embedded object with a $K - [60]$ color of 13.3 mag. The brighter CTTS would be found in the brighter clump of young candidate objects, were it at the Perseus distance. The fainter, more embedded object would appear on the bright side of the clump that is more consistent with SWIRE galaxy colors. Therefore, some of the objects with colors consistent with SWIRE galaxies could also be candidate YSOs; one cannot simply make a brightness cut to cleanly distinguish between YSOs and galaxies.

As with the 70 μm detections in Figure 8, here only the brighter objects are also detected at 160 μm. The effects of the bright neb-ulosity in the clusters are vividly apparent, as no objects in this plot in the clusters are also detected at 160 μm.

There are nine very red objects with $K_s - [70] > 15$ mag, a region of color space in which no background SWIRE galaxies

are seen. They are listed in Table 5. For some of these sources, 24 μm fluxes were not available due to saturation or extended emission.

3.3.3. *The* [24] *versus* [24] − [70] *Diagram*

Figure 11 is an all-MIPS CMD, presenting [24] versus [70] for objects in Perseus, and again, for comparison, objects in the full SWIRE survey. As in Figure 10, (1) the deeper SWIRE survey extends to bluer objects for the faintest 24 μm values in the Perseus survey; (2) objects found in Perseus with 24 μm and colors consistent with those found in SWIRE are potentially galaxies, although there are clearly objects in Perseus with redder colors for a given 24 μm flux density than are found in SWIRE; and (3) the brighter objects are likely to be cluster members.

The Perseus population from the rest of the cloud in Figure 11 does not have two clumps that are as distinct as those found in Figure 10; it is much more dispersed, both in the [24] and in the [24] − [70] directions. It is difficult to make comparisons between the clusters and the rest of the cloud because there are so few objects available in the clusters; as before, for IC 348 and NGC 1333, the brightness of the nebulosity enforces a brightness cutoff such
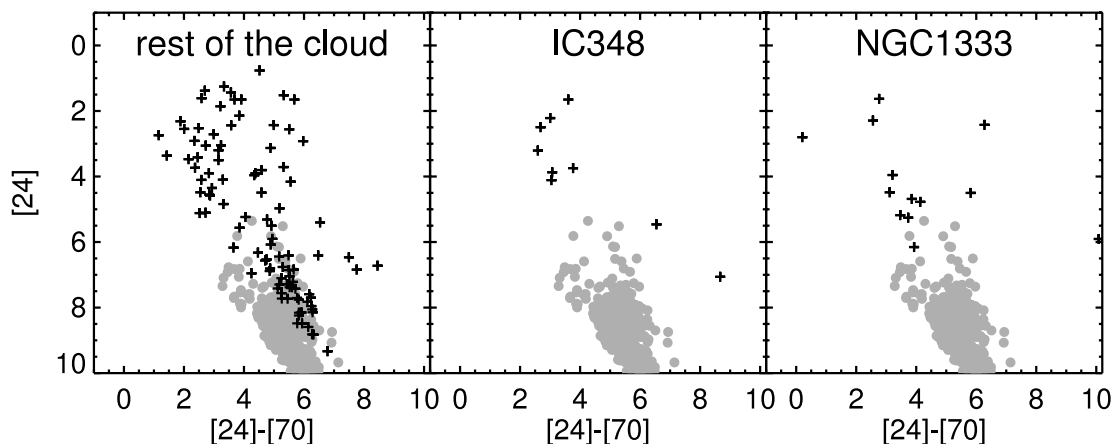

Fig. 11.—[24] vs. [24] − [70] CMD for Perseus (*plus signs*), with data for SWIRE (*filled gray circles*) included for comparison. As in Fig. 10, the fainter objects like those found in SWIRE correspond to extragalactic ([24] $\sim$ 7–10), and the brighter objects are YSO candidates ([24] $\lesssim$ 5); there are few faint objects in the clusters because the bright nebulosity there limits the survey sensitivity. Very red sources ([24] − [70] > 6) are the most embedded objects; note the NGC 1333 object near [24] − [70] = 10.1. The Perseus YSO population in the rest of the cluster is more dispersed (toward the upper right) than in the clusters or lower on the diagram; this suggests young and/or embedded objects, or there could be a significant dispersion in distance to the objects.
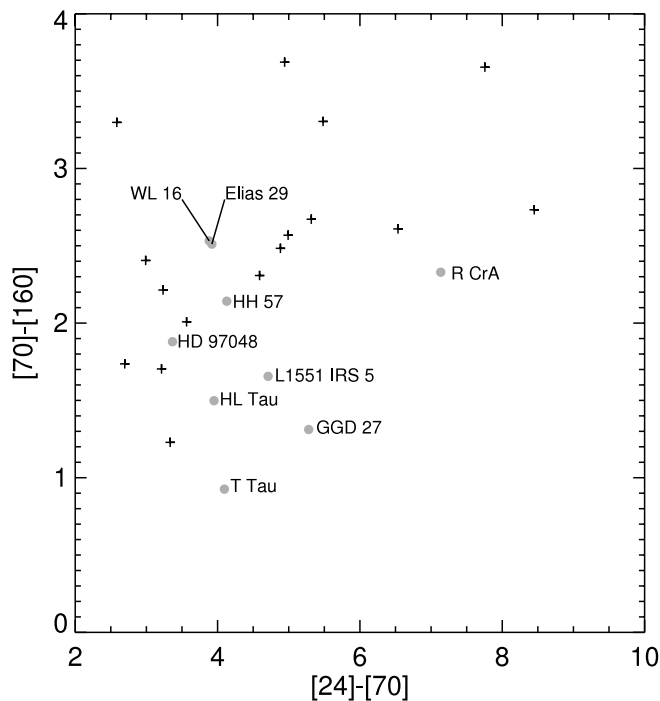
FIG. 12.—MIPS color-color diagram for objects in Perseus (*plus signs*) and for a variety of well-studied objects (*filled gray circles*; A. Noreiga-Crespo 2005, private communication). The colors of these objects in Perseus are consistent with young objects.

FIG. 13.—Locations of all sources in the 24 μm catalog (*small dots*), sources detected at 160 μm (*plus signs*), and those detected at all three MIPS bands (*additional solid boxes*). The rest of the notation is as in Figs. 1 and 9. Most of the objects are within the IRAC map, e.g., within the region of highest extinction. Objects detected at all three MIPS bands are discussed individually in § 4.2.

that there are few faint and red objects detected. The nebula is bright enough that it also limits the number of brighter legitimate cluster members that can be detected in this parameter space. Certainly a young and/or embedded population is present in the rest of the cloud. A significant distance dispersion could broaden the distribution of objects seen in the rest of the cloud in comparison to the clusters, or the increased number of objects could simply better represent the true distribution of young objects. At the faintest levels, the reddest SWIRE objects are found near $[24] - [70] \sim 7$, so the handful of objects found to be redder than that are likely to be cloud members and highly embedded.

There are five very red objects with $[24] - [70] > 7$ mag, and they appear in Table 5. They are all young, very embedded objects. SSTc2d 032910.5+311330 is by far the reddest object, with $[24] - [70] = 10.1$; its position is consistent with IRAS 4A1/4A2 in NGC 1333, which is indeed a well-known embedded object (see, e.g., Reipurth et al. 2002; Choi 2005; Rebull et al. 2003; Mott & Andre 2001 and references therein). Although this object is clearly detected in 70 μm, the IRAS 4B and 4C components are nearby and also clearly detected, so the 70 μm flux as measured for IRAS 4A may have imperfectly accounted for contributions from IRAS 4B and 4C, affecting the $[24] - [70]$ color as measured.

3.3.4. *The* $[70] - [160]$ *versus* $[24] - [70]$ *Diagram*

Figure 12 shows the MIPS color-color diagram for Perseus. Included for comparison on this plot are colors calculated for MIPS bands from *Infrared Space Observatory* (*ISO*) SWS data for a variety of very famous well-studied embedded objects from A. Noriega-Crespo (2005, private communication). This parameter space has not been commonly explored until very recently, in part because the "famous" regions of most clusters have bright enough nebulosity (as we do in our clusters here) so as to preclude detection at at least one of the three MIPS bands. In the case of Perseus, the large area we have covered with our MIPS map includes many interesting objects in regions beyond the famous
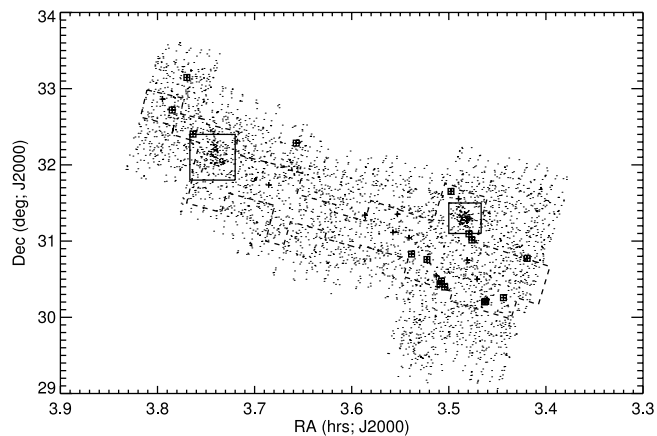
clusters. All of the Perseus objects in Figure 12 are from the rest of the cloud where the nebulosity is low enough to enable measurements at all three MIPS wavelengths; the colors of these objects, despite being from the rest of the cloud, are clearly consistent with being young stars. The locations of these objects are shown in Figure 13. Only one object is detected at 160 μm within our defined cluster regions (it is in NGC 1333; see Fig. 13), and that object has no measured (e.g., unsaturated) counterpart in the catalog at 24 and 70 μm. We expected that none of these objects are likely to be extragalactic in that the sensitivity of our 160 μm survey is such that it is really only likely to probe Galactic objects, e.g., cluster members. However, one object may be extragalactic; see § 4.2, which discusses each of these objects detected at all three MIPS bands.

There are several objects detected at the longer MIPS bands but lacking counterparts at the shorter MIPS bands. These could be indicative of very embedded objects, but because our survey becomes shallower and shallower at longer wavelengths, they are also often objects where the shorter wavelength counterpart is simply saturated. There are 18 objects with 70 μm measurements but no 24 μm counterparts; four of note appear in Table 5. As can be seen in the table, most of these objects fall into one of two categories: objects that are saturated at 24 μm (10 of these, most of which are in NGC 1333) and objects that are faint and/or extended at 24 μm (four objects). The last of these objects, LkHa 325, is relatively isolated and seems to have a 70 μm PSF peak slightly offset from the 24 μm peak; this could be an instrumental effect in that the detection is on the edge of a scan leg, which could affect the centering of the detection.

Finally, we looked for objects with 160 μm measurements but no 24 or 70 μm counterparts; there are eight such objects, and they appear in Table 5. Five of these objects are saturated at the shorter wavelengths. Two objects are diffuse and the center of their 160 μm emission is clearly offset from the center of a nearby star seen at the shorter wavelengths. We suspect that the emission in these cases arises in a clump of ISM material heated by an adjacent stellar source.

3.4. 24 μm *Variability*

To reject asteroids, two 24 μm observations separated by 3–6 hr were made for every position in the MIPS Perseus map. This data set provides an opportunity to search for time variability of cloud members and extragalactic background sources on this timescale. Figure 14 shows the ratio of flux densities measured at the two
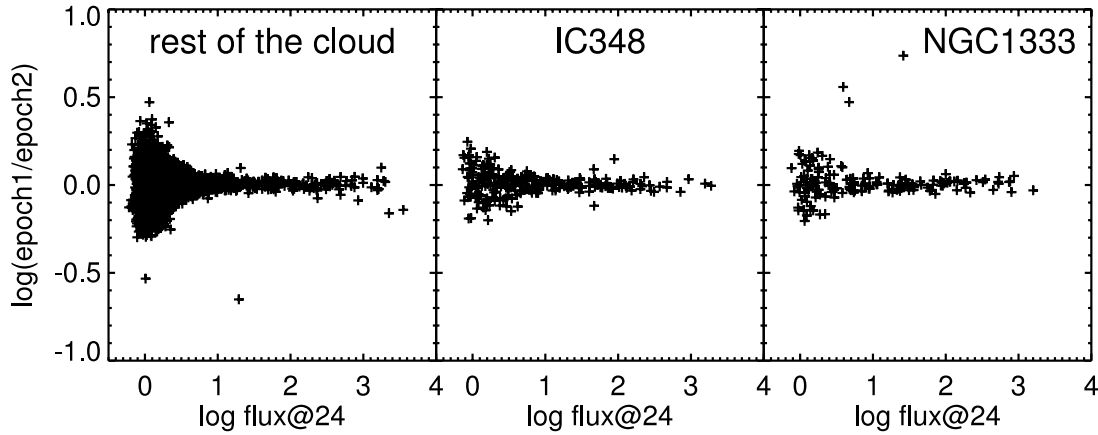
FIG. 14.—Search for time variability at 24 μm. All of the outliers are explicable in terms of image defects or extended sources; see text. There is no real variability of any of the 24 μm sources in our field on timescales of $\sim$6 hr to $\sim$10%.

epochs, as a function of the combined 24 μm flux density. The results show an rms difference of $\sim$10% between epochs, consistent with our expected measurement uncertainties. Below flux densities of 10 mJy, the detected signal-to-noise ratio falls below 10, and the dispersion between the measurements increases accordingly. Several objects appear as outliers from this general distribution. Investigation of these individually shows that they suffer from one of several defects: they fall on the edges of the map (where photometry is less reliable), are contaminated by artifacts from nearby bright objects (as in the case of NGC 1333), are confused by bright extended emission, or are extended and thus not measured accurately by our point-source fitting photometry. The apparent variability in all these cases is therefore of instrumental origin. We therefore conclude that none of the $\sim$4000 24 μm sources in Perseus show real variability above the 10% level on timescales of 3–6 hr.

3.5. *Large-Scale Extended Emission*

Bright extended emission is present at all three wavelengths throughout the MIPS Perseus mosaics (Figs. 2–5). While MIPS has much more sensitive detectors than *IRAS* had, it also samples much smaller pixel/beam sizes. The result is that in our MIPS fast scan observations, the achieved surface brightness sensitivity is only incrementally better than that of *IRAS*, and the majority of the extended structures we see have direct counterparts in the *IRAS* maps. The major value added by the MIPS observations is a factor of 3–5 better spatial resolution, enabling studies of structural detail in the extended emission. A drawback is that MIPS saturates on the extended emission in parts of IC 348 and NGC 1333 at 70 and 160 μm.

At 24 μm (Fig. 2), the brightest extended emission is seen on the east side of the cloud complex where several B stars act as illuminating sources. The largest single feature is the 1.4° diameter *IRAS* ring illuminated by HD 278942 (Andersson et al. 2000; Ridge et al. 2006). Even with the added resolution supplied by MIPS, the ring edges remain diffuse, unlike a swept-up shell. A prominent 24 μm nebulosity surrounds the central star and is discussed further in § 4.4. A second, much smaller ring appears within the larger one. Its center is offset to the east by 7′, and it appears to be illuminated by the *IRAS* source 03382+3145. Bright emission in IC 348 takes the form of a large cavity open to the northwest, again with diffuse edges. The peculiar structure in the 24 μm nebulosity at the center of IC 348 is discussed below (§ 4.3). With the exception of local nebulosities illuminated by

BD +30 549 (in NGC 1333) and BD +30 540 (see § 4.5), there is very little 24 μm extended emission in the west side of the cloud complex.

At 70 μm (Fig. 3), the extended emission structure is similar to that seen at 24 μm. One important difference is that the nebulosity around HD 278942 fades considerably. Streaking artifacts appear along the scan direction after a scan crosses over a bright source.

At 160 μm (Fig. 4), however, a wealth of new structure appears in the extended emission. On the west side of the cloud complex, a bright filament appears along the B1 submillimeter ridge (Enoch et al. 2006) and extends southwest to the Per 6 stellar aggregate (see § 4.1.1). Another large filament of 160 μm emission extends northeast to southwest across NGC 1333 and continues down toward L1455. There is extended emission around L1448. Just south of IC 348, an east-west region of 160 μm emission becomes prominent, offset from the 24 μm emission in the direction away from the illuminating stars. To appear so prominently at 160 μm while going largely unseen at 24 and 70 μm, these regions must trace cold cloud material. This is confirmed by a comparison of the distribution of 160 μm emission to the contours of visual extinction (Fig. 15; J06; Enoch et al. 2006). The extinction follows the 160 μm emission closely, except for the large ring illuminated by HD 278942. The extended emission around this star, which was so bright at 24 μm, is not detected at 160 μm.

Finally, the 160 μm extended emission also highlights the presence of three large voids on the west side of the Perseus cloud complex. The darkest of these is centered at $\alpha = 03^h35^m40^s$, $\delta = +31°50'$; two others are present at $\alpha = 03^h31^m$, $\delta = +31°$ and $\alpha = 03^h27^m10^s$, $\delta = +30°30'$ (between L1455 and L1448). These voids have characteristic sizes of $\sim$0.7° (3 pc at a distance of 250 pc). Smaller voids are also present. The absence of young stars and extended emission in these voids, and the corresponding concentration of star formation along the nearby extended emission/extinction filaments, is similar to what is seen in the Taurus molecular clouds (Hartmann 2003).

4. RESULTS AND DISCUSSION FOR INDIVIDUAL REGIONS AND OBJECTS

This large map is incredibly rich in interesting objects and features. In this section we select several objects or small groups of objects to discuss in more detail. Figure 16 shows the locations of these specific objects within the overall Perseus cloud. Table 6
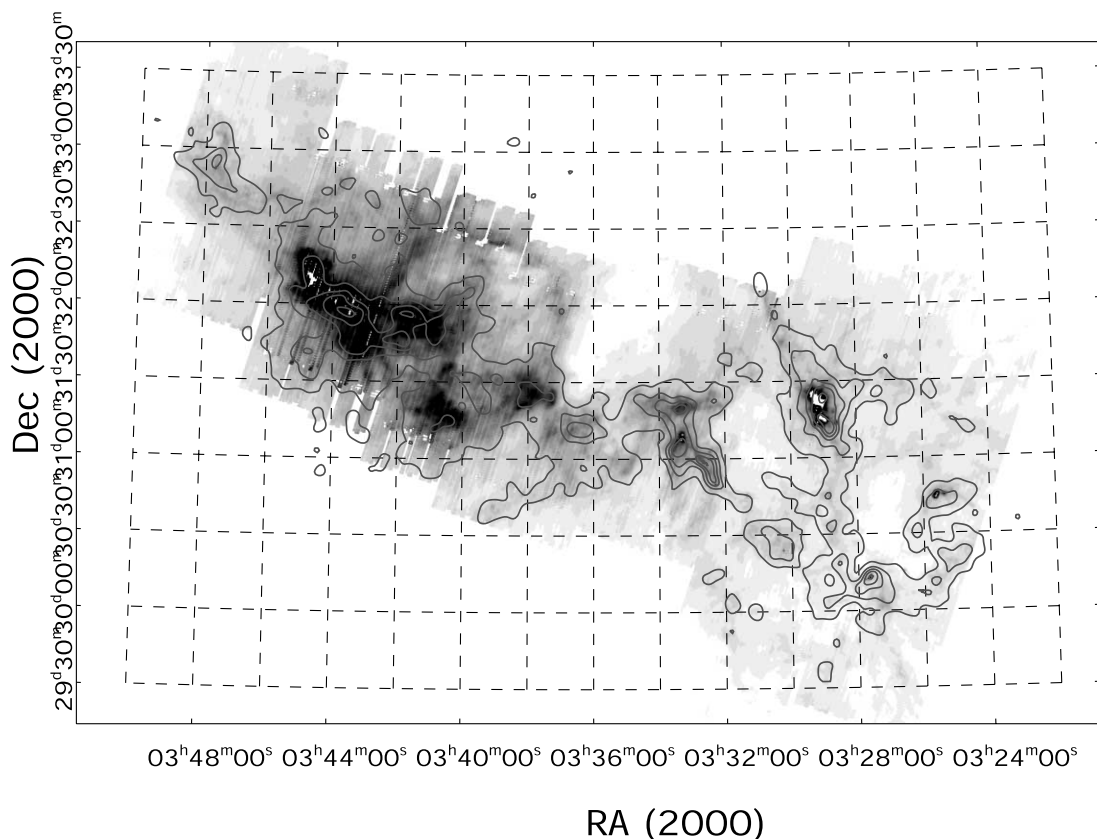
FIG. 15.—Mosaic of MIPS data at 160 μm (*gray scale*) with A_V contours overlaid (A_V levels are 2, 4, 6, 8, 10, 15, 20, 25, 30, 35, and 40 mag; see J06 and Enoch et al. [2006] for more discussion on A_V). The 160 μm emission closely follows the A_V, except in the large ring illuminated by HD 278942; see text.

lists the MIPS flux densities for the point sources discussed here (IRAC flux densities are available from the online c2d delivered catalogs). A_V estimates for individual stars were made using the method described in Evans et al. (2005). The SEDs presented below are all in λF_λ in cgs units (ergs s^{-1} cm^{-2}), against λ in μm. In these SEDs, we have included the 2MASS and IRAC data from J06 but have not comprehensively included every other flux mea-

surement from the literature of these objects, if relevant; some objects presented here are entirely new. Some objects whose SEDs are presented here were mentioned in J06, but their SEDs were deferred for presentation until this paper.

4.1. *Spectral Energy Distributions in Young Stellar Aggregates*

The term "stellar aggregates" was originally coined by Strom et al. (1993) in their NIR study of the young stellar population of the Orion L1641 cloud. They defined them as "regions of enhanced stellar surface density"—"sparse groups . . . likely to be gravitationally unbound, transient structures." They applied the term to isolated stellar groups <1 pc in size ($14'$ at the assumed distance of Perseus) and with as many as several dozen members. Their underlying assumption was that the aggregate members were born contemporaneously (i.e., are coeval) from a single parent molecular cloud core.

Throughout the Perseus map and outside the two large clusters, there are several small groups of 24 μm sources that fit the above definition of a stellar aggregate. In some of them, the stars are distributed in small linear strings or arcs, similar to those seen in NGC 2264 (Teixeira et al. 2006). The distribution of stars often follows structure in the millimeter continuum and 160 μm emission (see Fig. 5). In this section we discuss three new aggregates of stars, two of which appeared to the *IRAS* survey as single objects.

4.1.1. *Per 6: A New Aggregate between L1455 and B1*

There is a ridge of molecular gas that extends southwest from B1 toward L1455. Roughly in between B1 and L1455, Ladd et al. (1994) find an ammonia core they dubbed Per 6. Olmi et al. (2005) find here two cores, an N$_2$H$^+$ core and, slightly offset, a CS
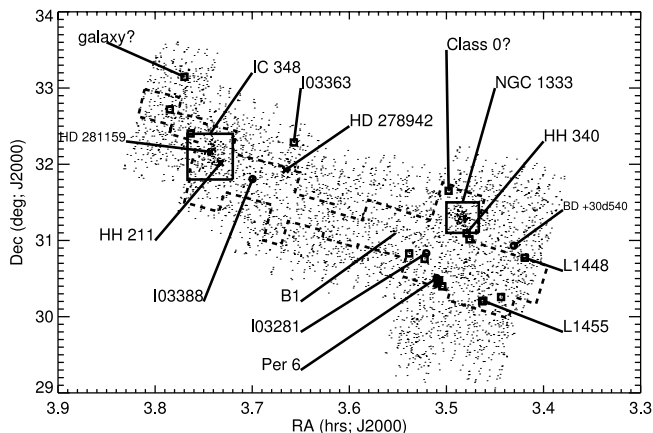

FIG. 16.—Locations of all objects in MIPS-24 catalog (*small dots*) and objects discussed in § 4. Most of the rest of the notation is as in previous figures (Figs. 1, 9, and 13), but here squares are objects detected at all three MIPS bands, crosses denote specific individual objects, and circles denote small groups of objects, all of which are discussed in § 4. (Note that Per 6, which has a circle because it is a small group, also has several objects detected at all three bands and thus plotted as squares.) Object names are given in most cases; to conserve space, *IRAS* sources are abbreviated "I" followed by the first 5 digits of the formal name.

TABLE 6
MIPS Photometry for Objects Discussed in § 4

SSTc2d Name	MIPS-24[a] (mJy)	MIPS-70[a] (mJy)	MIPS-160[a] (mJy)	Other Names	Notes
				New Aggregate near Per 6	
033015.1+302349	1900.0	5499	7170	IRAS 03271+3013	#1 in § 4.1.1
033027.1+302829	431.0	920	1450	IRAS 03273+3018, HH 369	#2 in § 4.1.1
033030.2+302708	48.9	. . .	. . .		#3 in § 4.1.1
033032.7+302626	31.1	320	1960		#4 in § 4.1.1
033035.9+303024	572.0	180	. . .	IRAS 03275+3020, GSC 02342−00390, AX J0330.5+3030	#5 in § 4.1.1
033036.7+302735	3.9	. . .	. . .		#6 in § 4.1.1
033036.9+303127	322.0	130	. . .		#7 in § 4.1.1
033038.2+303211	57.5	260	. . .		#8 in § 4.1.1
033044.0+303246	699.0	750	. . .	LkHa 326=HBC 14 =IRAS 03276+3022	#9 in § 4.1.1
033054.5+303146	1.0	. . .	. . .		#10 in § 4.1.1
				IRAS 03388+3139 Stellar Aggregate	
034155.0+314939	1.0	. . .	. . .		#1 in § 4.1.2
034155.7+314811	120.0	. . .	. . .		#2 in § 4.1.2
034157.4+314836	264.0	. . .	. . .		#3 in § 4.1.2
034157.7+314800	112.0	. . .	. . .		#4 in § 4.1.2
034158.5+314855	345.0	. . .	. . .		#5 in § 4.1.2
034158.6+314821	36.5	. . .	. . .		#6 in § 4.1.2
034201.0+314913	4.8	. . .	. . .		#7 in § 4.1.2
034202.1+314801	115.0	. . .	. . .		#8 in § 4.1.2
034204.3+314711	22.2	. . .	. . .		#9 in § 4.1.2
				IRAS 03281+3039 Stellar Aggregate	
033110.7+304940	62.0	. . .	. . .	LZK 19	#1 in § 4.1.3; mentioned in J06
033114.7+304955	229.0	220	. . .		#2 in § 4.1.3; mentioned in J06
033118.3+304939	292.0	230	. . .	LZK 20	#3 in § 4.1.3; mentioned in J06
033120.1+304917	15.0	. . .	. . .		#4 in § 4.1.3; mentioned in J06
				Objects Detected at All Three MIPS Bands	
032509.4+304622	2000.0	2600	2640	LDN 1448 IRS 1	Discussed briefly in J06; see § 4.2
032637.4+301528	400.0	3900	7880	IRAS 03235+3004	Discussed in J06
032743.2+301228	761.0	8190	17900	LDN 1455 IRS 4	Discussed in J06
032747.6+301204	1620.0	1900	8130	IRAS 03247+3001, L1455 IRS 2	Discussed in J06; see § 4.2
032834.5+310051	1290.0	2700	2660	IRAS 03254+3050	See § 4.2
032845.3+310541	215.0	1600	2750	HH 340	See § 4.2
032951.8+313905	49.3	2200	4990	IRAS 03267+3128	See § 4.2
033015.1+302349	1900.0	5499	7170	IRAS 03271+3013	See #2, § 4.1.1
033027.1+302829	431.0	920	1450	IRAS 03273+3018, HH 369	See #5, § 4.1.1
033032.7+302626	31.1	320	1960	. . .	See #7, § 4.1.1
033121.0+304529	14.6	3800	9660	IRAS 03282+3035	Discussed in J06
033218.0+304946	13.1	1800	10700	IRAS 03292+3039	Discussed in J06
033925.5+321707	234.0	3400	8170	2MASS 03392549+3217070, IRAS 03363+3207	See § 4.2
034548.2+322411	2250.0	5265	3350	LkHa 330	Discussed in Brown et al. (2007)
034611.0+330848	19.5	330	1420	2MASS 03461106+3308488	Galaxy
034705.4+324308	587.0	1000	1880	IRAS 03439+3233, B5 IRS 3	Discussed in J06; see § 4.2
				Other Individual Point Sources	
032548.9+305725	197.0	290.0	. . .	LZK 5	§ 4.5
032533.2+305544	64.8	86.0	. . .	LZK 2	§ 4.5
032552.8+305449	64.5	. . .	. . .	. . .	§ 4.5
032548.1+305537	∼100	1200.0	. . .	BD +30 540, SAO 56444, IRAS 03227+3045	
033955.6+315533	62.5	. . .	. . .	HD 278942, IRAS 03367+3145	§ 4.4

[a] Absolute uncertainties on the 24 μm data are estimated to be 10%–15%; statistical uncertainties are much less than this. Uncertainties on 70 and 160 μm flux densities are estimated to be 20%.
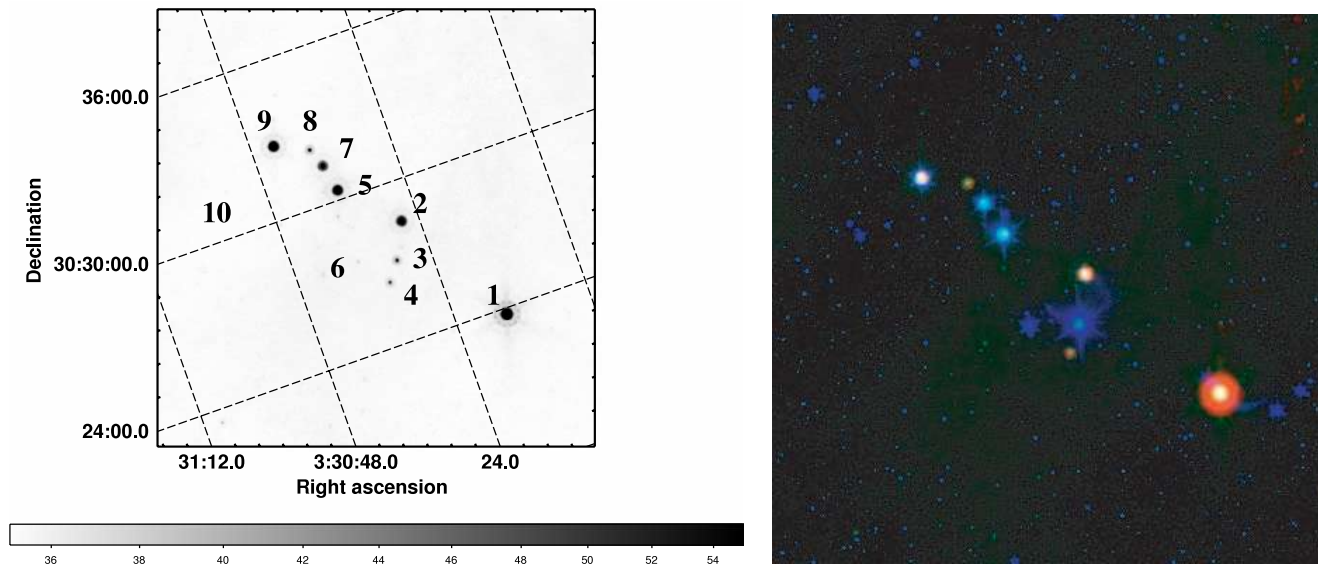
Fig. 17.—Per 6, a new aggregate of objects bright at MIPS wavelengths. All of the objects are within $11' \times 2.5'$. *Left*: Gray scale of the 24 μm image with sources numbered to correspond to discussion in text. *Right*: Three-color image with IRAC 4.5 μm (*blue*), MIPS 24 μm (*green*), and MIPS 70 μm (*red*), all log scale. Note extended emission around source 1 in IRAC.

core. Hatchell et al. (2005) find an 850 μm core here (No. 81); Enoch et al. (2006) find three millimeter continuum cores in this region (Bolo 60, Bolo 61, Bolo 62). Based on submillimeter continuum and NIR extinction maps, in between Enoch's Bolo 61 and Bolo 62, Kirk et al. (2006) find what they dub an "extinction core" (their No. 25) and an "extinction super core" (their No. 6). The Per 6 region also contains four *IRAS* sources, IRAS 03271+3013, IRAS 03273+3018, IRAS 03275+3020, and IRAS 03276+3022.

In this Per 6 region, there is a grouping of 10 objects detected at MIPS wavelengths, 8 of which are bright at 24 μm, 7 of which are detected at 70 μm, and 3 of which are detected at 160 μm.

Figure 17 contains a 24 μm image and a key to object numbers for this discussion, as well as a three-color image using 4.5, 24, and 70 μm. SEDs for all of these Per 6 components can be found in Figure 18. There is a diversity of SED types present here, ranging from apparent photospheres to Class 0 candidates. In addition, there are eight objects in this region with similar SEDs, which are very faint at all available bands and undetected by 2MASS; these objects are most likely background galaxies, so they are not included in the subsequent discussion here.

All of the bright objects are located within a region $11' \times 2.5'$ (0.8×0.2 pc at a distance of 250 pc). The positions of the Ladd et al. (1994), Olmi et al. (2005), and Hatchell et al. (2005) cores
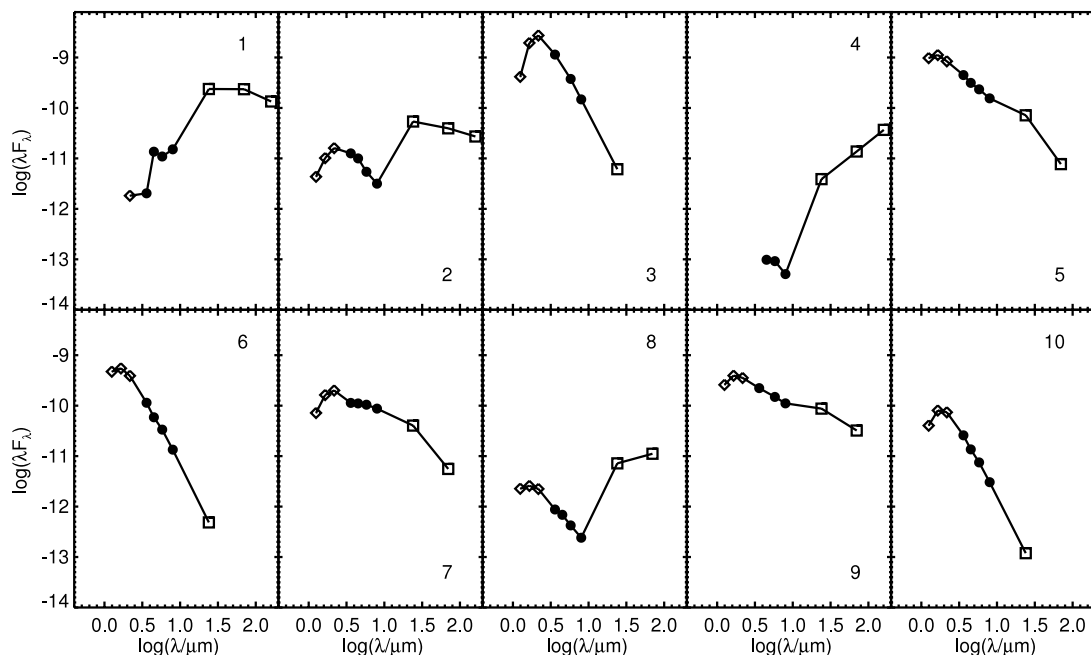
Fig. 18.—SEDs for the 10 components of the new Per 6 aggregate. Diamonds are 2MASS detections, circles are IRAC detections, and squares are MIPS detections. The units of λF_λ are cgs (ergs s^{-1} cm^{-2}); it is plotted against λ in μm. The objects here have diverse SEDs; some objects (like 6) are photospheres, some objects (like 2) clearly have circumstellar disks, and some objects (like 1) are deeply embedded.

are coincident with source 1, the brightest 24 μm source in the grouping, so we refer to this new aggregate of young objects as "near Per 6," or simply "Per 6."

Enoch et al. (2006) found three cores here, one of which, Bolo 60, is coincident with source 1. Core Bolo 62 is coincident with source 4, and the core Bolo 61 is not coincident with a 24 μm source; it is about an arcminute southwest of source 2 and about an arcminute west of source 3. Texture in the millimeter map from Enoch et al. (2006) reveals additional structure in the extended dust continuum emission that threads between sources 2 and 5, curving back around to source 9; a similar structure can be seen in the 160 μm emission.

The brightest object at 24 μm, object 1, can be identified with IRAS 03271+3013, which was seen in Aspin (1992) as a bipolar outflow source and listed in Ladd et al. (1993) as a young object. It is a point source in all three MIPS wavelengths but has "cometary" morphology in IRAC, such that there is diffuse emission coming off of one side of the IRAC source (see Fig. 17). J06 finds that deeply embedded objects often have extended emission in one or more IRAC bands, lending support to the idea that this object is deeply embedded. This object is bright enough to be detected at all three MIPS bands (see Fig. 18). Most of the energy is being emitted at the longest wavelengths, consistent with an embedded very young object. It is one of the reddest dozen objects seen in Figure 8 with $K_s - [24] > 9.7$ mag, and also one of the reddest objects seen in Figure 10 with $K_s - [70] > 15$ mag. It does not have a smooth SED at IRAC wavelengths, possibly because the image is slightly extended, which leads to errors in our PSF fitting photometry. As mentioned above, the position for this object is consistent with cores measured at long wavelengths such as the millimeter continuum observations in Enoch et al. (2006).

The position for IRAS 03273+3018 is consistent with both the position given in the literature for HH 369 and our *Spitzer* detection No. 2. The position given for HH 369 (Alten et al. 1997) is 4″ north of the MIPS position. The object found at this location is a point source at MIPS wavelengths, but slightly extended in IRAC-2, as can be seen in Figure 17. The position given for HH 369 is in the direction of a slight extension of the IRAC image, but still within the extent of the object as seen in Figure 17. The SED for this object, as can be seen in Figure 18, includes all three MIPS bands and has most of the energy being emitted at the longer wavelengths. The shape of the SED at the long wavelength end is consistent with being composed of photosphere plus strong long-wavelength excess, consistent with a YSO seen only via scattered light at short wavelengths. Source 2 is thus presumably the protostar driving the HH 369 outflow.

Object 4 has no known literature counterpart. It is the third (of three) objects in this aggregate detected at all three MIPS bands. It has a very steep SED (Fig. 18), with only marginal detections at the three longest IRAC bands, and no IRAC-1 or 2MASS counterparts at all. This SED resembles that found for IRAS 03282+3035, discussed below in § 4.2 and in J06 as an outflow-driving source, except that this SED does not level off by 160 μm. This is evidently a deeply embedded object. The similarities between the morphology at IRAC bands and the SED of this object and IRAS 03282+3035 suggest that this new object may also be a Class 0 object.

Object 5 can be identified with IRAS 03275+3020, which is optically visible as GSC 02342−00390 and the *ASCA* X-ray source AX J0330.5+3030 (Yamauchi et al. 2001). Yan et al. (1998) identify this object as a Class I object; Yamauchi et al. (2001) identify their X-ray detection with the *IRAS* source and classify it as a T Tauri object. The SED that can be seen in Figure 18 suggests that it is certainly a Class II object.

Object 9 is consistent with the position for IRAS 03276+3022, which appears in Ladd et al. (1993) as a candidate young object. This same object is identified with LkHa 326 and HBC 14 (Casali & Eiroa 1996), an emission-line star in Liu et al. (1980), and even a candidate active galactic nucleus (AGN; de Grijp et al. 1987). Based on the SED seen in Figure 18, we suggest that it is an embedded young object, perhaps a Class II.

Objects 7 and 8 also have no known literature counterparts. Object 7 has an SED consistent with that for a young and/or embedded Class II object. Object 8 has an SED where most of the energy is emitted at the longer wavelengths, suggesting a classification similar to object 2 in this same aggregate.

Objects 3, 6, and 10 are all consistent with photospheres, with no known counterparts in the literature. They are distributed along the ridge of 160 μm emission, suggesting that they are Perseus members. The Wainscoat et al. (1992) Galactic star count models predict a 70% chance that a background source with a 24 μm flux density as faint as object 10 should randomly fall within the area of the Per 6 aggregate. While this object is probably not a Perseus member, the same analysis gives probabilities of just 20% and 3% that objects 6 and 3 are part of the background Galactic population. Object 3 has the highest extinction of these three, with an estimated A_V of 15 mag; object 6 has A_V of about 4 mag, and object 10, 9 mag.

There are at least two different possible methods of classification of the objects in this aggregate. Based on the $K_s - [24]$ color, three objects (1, 2, 8) are Class I, three objects (5, 7, 9) are Class II, and three objects (3, 6, 10) are Class III. The remaining object (4) is not detected at K_s. Alternatively, we can classify objects based on a value of α fitted to the SED between K_s and 24 μm, following the original Greene et al. (1994) classification scheme, where $\alpha \geq 0.3$ is Class I, $-0.3 \leq \alpha < 0.3$ is "flat spectrum," $-1.6 < \alpha < -0.4$ is Class II, and $\alpha < -1.6$ is Class III. Using this classification, four of the objects (1, 2, 4, 8) are Class I, none are "flat-spectrum" objects, three objects (5, 7, 9) are Class II, and three objects (3, 6, 10) are Class III. The objects with available classifications based on $K_s - [24]$ color have the same classification using an α fit to the entire available SED.

This aggregate, while it spans ∼0.2 pc in the narrow dimension, is ∼0.8 pc in the long direction, larger than the average core size of ∼0.08 pc found by Enoch et al. (2006). Objects 2, 3, 4, and 6 and a millimeter continuum core without a 24 μm counterpart from Enoch et al. (2006) are all within ∼2.3′ (∼0.2 pc); even this subgroup has a diversity of SEDs. An apparently starless millimeter continuum core and two of the most embedded objects in this aggregate are found in close proximity to two of the least embedded.

4.1.2. *IRAS 03388+3139 Stellar Aggregate*

IRAS 03388+3139 was seen by *IRAS* as a single object, but MIPS reveals that there are actually at least nine objects seen at 24 μm here within a region 90″ in diameter (0.1 pc at a distance of 250 pc; see Fig. 19). The location of the original *IRAS* source is between sources 3 and 5 in this finder chart; the positional uncertainty encompasses both objects. This object also appeared as seen by *MSX* in Kraemer et al. (2003; it is listed as G160.2784−18.4216 and J034158.34+314852.6). There are no cores found by Enoch et al. (2006) or Hatchell et al. (2005) in this region.

As in Per 6, this aggregate of objects displays a striking variety of SEDs within this small region (see Fig. 20). Some objects resemble photospheres, most with long-wavelength excesses (1, 3, 4, 7, 8, and perhaps 5, if we had unsaturated JHK_s), and some (2, 6, 8) are clearly more deeply embedded. None of the objects are detected at 70 or 160 μm. Despite this, object 8 is one of the
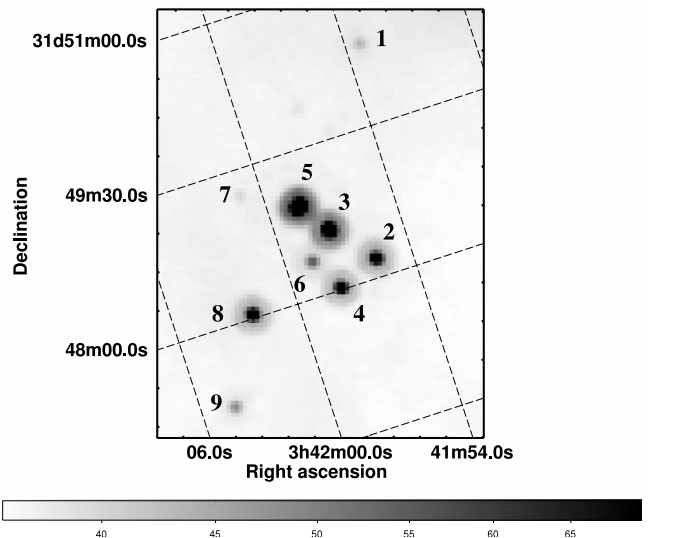
FIG. 19.—IRAS 03388+3139 resolves into several pieces within 90″ (diameter) when viewed by MIPS-24 (*gray scale*). The numbers correspond to the numbers used in the next figure, which presents SEDs.

reddest dozen objects in Figure 8 with $K_s - [24] > 9.7$ mag. Object 1 is the faintest of the group, with a nearly photospheric SED and an inferred $A_V \sim 11$ mag. The Wainscoat et al. (1992) models assign a 16% probability that a background source with the 24 μm flux density of object 1 would be found within the $4' \times 2'$ area of the aggregate.

As above, there are at least two different ways to classify these objects. A $K_s - [24]$ color is available for all but one of the objects; three objects (2, 6, 8) are Class I, four objects (3, 4, 7, 9) are Class II, and the last (1) is Class III. Based on a fit to the SED between K_s and 24 μm, similar classifications are obtained (only object 2 changes classification): two Class I objects (6 and 8), one flat-spectrum object (2), five Class II objects (3, 4, 5, 7, 9), and one Class III object (1).

4.1.3. *IRAS 03281+3039 Stellar Aggregate*

IRAS 03281+3039 is another object that, when viewed by MIPS, is resolved into multiple sources (see Fig. 21). (This object was also mentioned by J06; this aggregate of stars is located along the ridge of molecular emission between B1 and the Per 6 cluster discussed above.) There are four components to this object seen at MIPS-24 (two of which are also seen at 70 μm) within 120″ diameter, or 0.15 pc at a distance of 250 pc. The *IRAS* position is located at a position equidistant from the three brightest objects seen in Figure 21, with a position uncertainty nearly reaching across from source 1 to 3. There are no cores found by Enoch et al. (2006) or Hatchell et al. (2005) in this region.

As mentioned in J06, de Grijp et al. (1987) list this as an AGN candidate, but we suspect, based on the SEDs seen in Figure 22, that it is instead a small grouping of young stars. Objects 1, 3, and 4 look like photospheres plus circumstellar dust; object 2 seems to be the most embedded. As above, there are several different ways to classify these objects. The classifications based on $K_s - [24]$ and on a fit to the SED between K_s and 24 μm produce identical classifications; all are Class II, except object 2, which is a flat-spectrum object.

Objects 1 and 3 can be identified with emission-line stars in Liu et al. (1980). HH 770–HH 772 can be seen in this vicinity in the IRAC-2 image, suggesting recent jet activity in this area. On the whole, these objects appear to be less embedded than the ob-

jects from IRAS 03388+3139 or Per 6 above. The inferred A_V for these objects ranges from ~6 to ~12 mag.

4.1.4. *Comments on the Aggregates*

Three new aggregates of young stars have been discussed above. In all three cases, follow-up data will be required to better define their SEDs, establish their multiplicity, and measure their spectral types and presence of accretion diagnostics. However, the facts that most of the sources are bright at 24 μm, that they have high inferred extinctions, and that they have infrared excesses reminiscent of known YSOs suggest that they are indeed YSOs. They are all in close clumpings (within ~0.1 pc[21]); these and other similar groupings can be seen in the full Perseus map (Fig. 2), usually following the filamentary structure found in the 160 μm emission (Fig. 5). A similar spatial relationship between strings of young stars and molecular cloud filaments has also been seen in NGC 2264 (Teixeira et al. 2006). The typical nearest neighbor distances within the aggregates are 0.08, 0.04, and 0.05 pc for Per 6, IRAS 0338+3139, and IRAS 03281+3039, respectively, very similar to the 0.08 pc spacing found in the NGC 2264 "spokes cluster," which Teixeira et al. (2006) identify with the Jeans length for thermal fragmentation of the molecular cloud filaments.

Each of the Perseus aggregates contains objects in close physical proximity and with a wide diversity of SEDs. In this, they are reminiscent of the L1228 South aggregate identified in *Spitzer* data by Padgett et al. (2004), where highly embedded objects, objects with substantial disks, objects with debris disks, and photospheres were all found in an aggregate of nine bright 24 μm sources within a region of $d < 1$ pc. The potentially youngest object found in the Perseus aggregates is a cold millimeter continuum core from Enoch et al. (2006). The earliest class of object seen at 24 μm is Class I. The latest class found in these aggregates is Class III. This wide range of circumstellar environments present within a compact (and presumably related) group of young stars raises interesting questions about star formation and circumstellar disk evolution.

There are two possible formation scenarios that could account for the diversity of SEDs in these aggregates. The first is that every source spends a relatively fixed fraction of its life in each of the Class 0, I, II, and III phases of protostellar evolution. In this scenario, the observed diversity of SEDs would require a significant age spread among the members of the aggregates. The second possibility is that the aggregate members formed at roughly the same time (i.e., are coeval), and that the process of circumstellar evolution proceeds at very different rates in different objects, such that some members evolve into Class III sources over the same timescale at which others remain Class I objects.

In the first scenario, if the aggregate members all started with similar initial conditions of mass, angular momentum, and initial cloud temperature (which is not unreasonable to assume, given their physical proximity), then to have both Class I objects and Class III objects in the same region requires some stars to be $\lesssim 0.1$ Myr old and some to be 1–5 Myr or possibly as much as 10 Myr old, assuming the canonical ages for objects in these SED classes (e.g., Bachiller 1996). If the Class III objects are not truly associated, leaving us with the Class II objects, then the oldest ages of objects in these aggregates are $\gtrsim 1$–5 Myr old, taking the

---

[21] IRAS 03388+3139 is ~0.1 pc, IRAS 03281+3039 is ~0.15 pc, and Per 6 is ~0.2 × 0.8 pc, larger than ~0.1 pc, but there is diversity of SEDs found even within a subgroup of size ~0.2 pc. Therefore, we are taking their typical size to be on the order of ~0.1 pc, not ~1 pc.
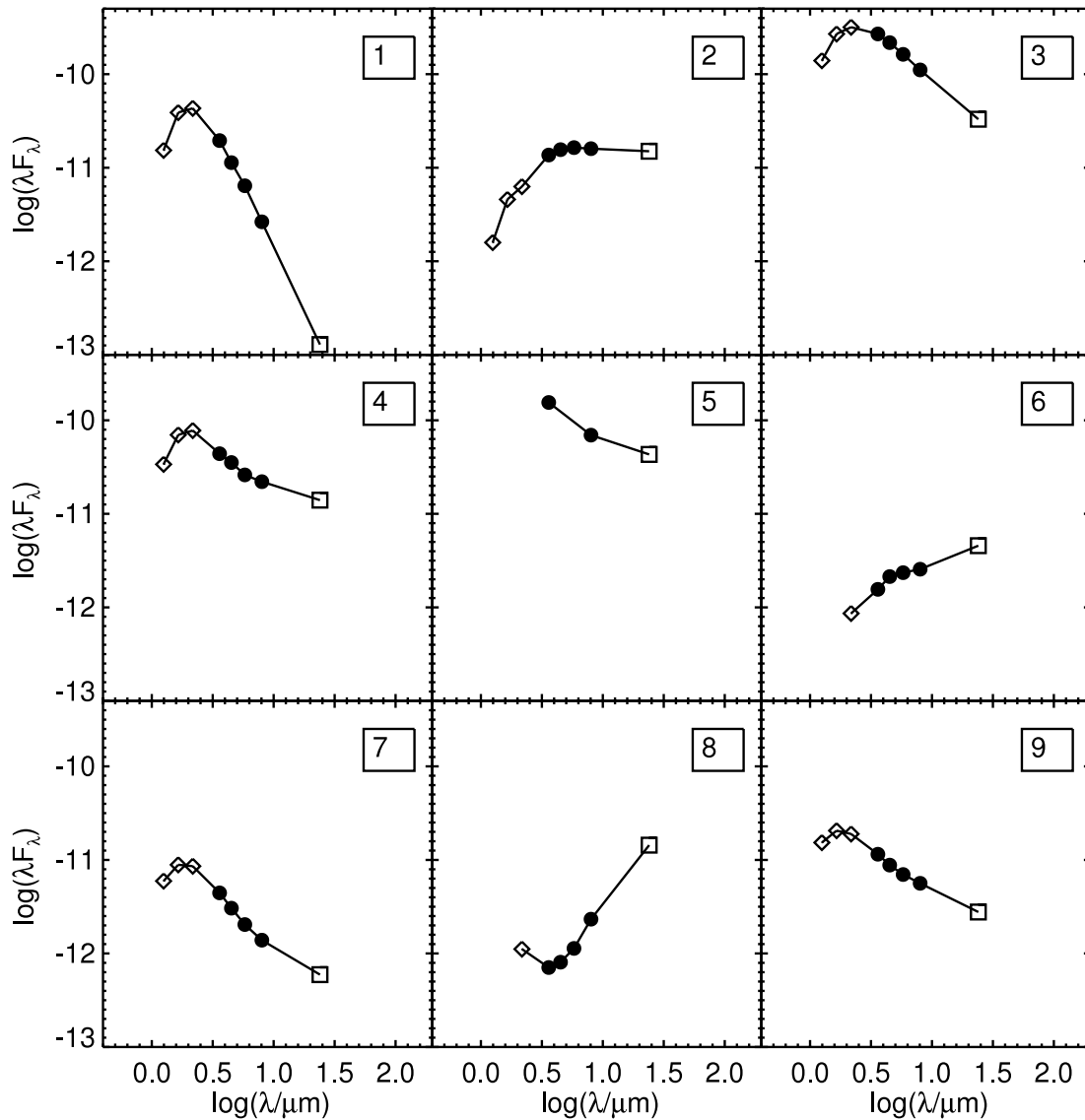
FIG. 20.—SEDs for the components of IRAS 03388+3139 within 90″ diameter. The numbers correspond to objects identified in the previous figure. All other notation is as in previous SED figures. There are a variety of SEDs found here, ranging from photospheric (object 1) to more embedded (object 2).
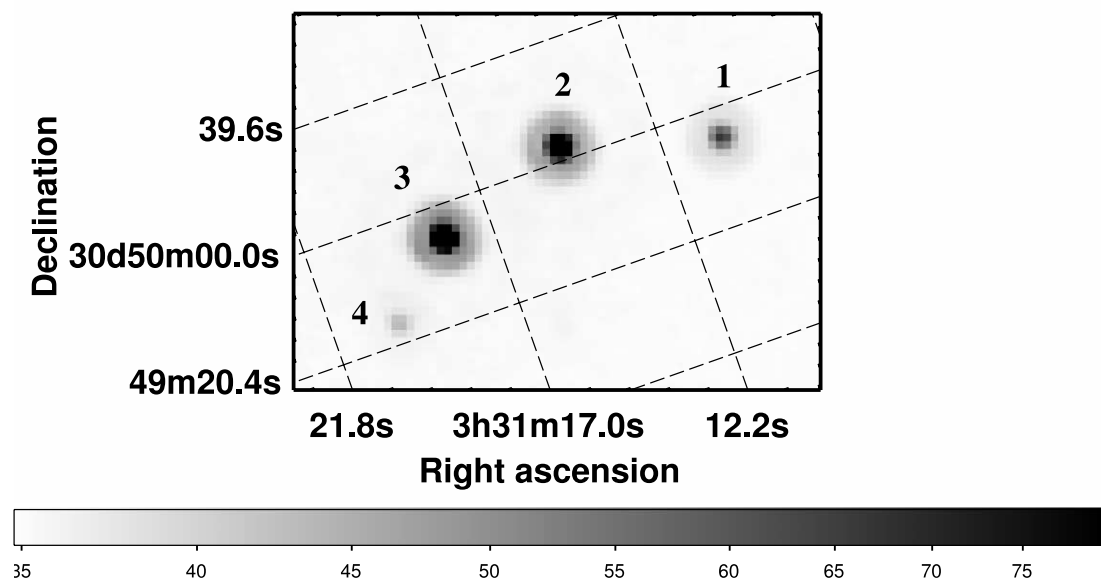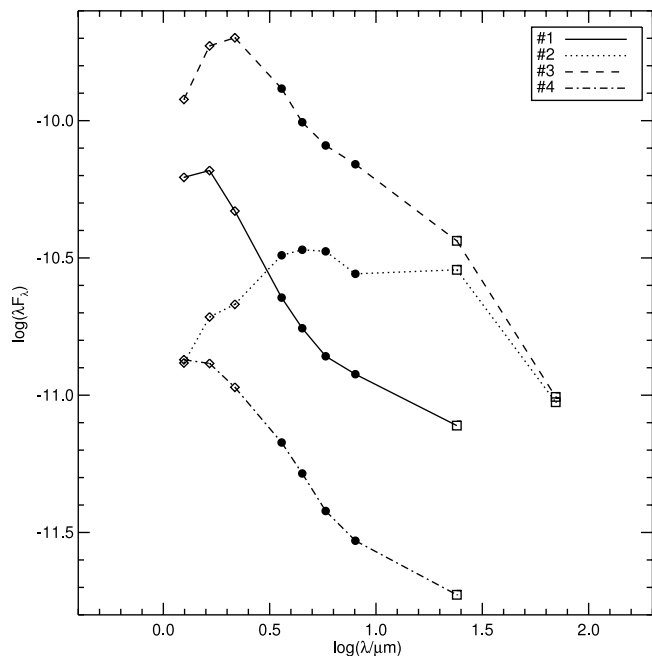

FIG. 21.—IRAS 03281+3039 resolves into several pieces within 120″ (diameter) when viewed by MIPS-24 (*gray scale*). The numbers correspond to the numbers used in the next figure, which presents SEDs.

Fig. 22.—SEDs for the components of IRAS 03281+3039 within 120″ diameter. The numbers correspond to objects identified in the previous figure. Notation is as in previous SED plots. In this aggregate, three of the four objects are close to photospheric; only one appears to have a substantial long-wavelength excess.

longest disk lifetimes to be between 1 and 5 Myr (see, e.g., Cieza et al. 2007; Rebull et al. 2004 and references therein).

On the other hand, if all of the objects were formed at very nearly the same time, which is also not unreasonable to assume based on their physical proximity, then there is a real diversity of evolutionary timescales for the various classes. A Class I object is often assumed to be much younger than a Class III object, and the timescale for the transition from Class I to Class III is usually taken to be long compared to the timescale for the transition from Class 0 to Class I. In order for these clumpings of stars to be the same age, the evolution of circumstellar matter around some objects must be fast, with the timescale to evolve from Class 0 to Class I comparable to the shortest possible time to evolve from Class 0 to Class III. Influences such as the system inclination, local stellar density and interactions between systems, initial disk mass (e.g., Beckwith et al. 2000), mass accretion rate and history (e.g., Calvet et al. 2005), initial core/clump and stellar rotation rate, and/or close binaries could all affect the disk/envelope dissipation timescale. An obvious follow-on investigation is an assessment of stellar multiplicity in the aggregates: if the Class III objects are preferentially binary, this could explain their more rapid circumstellar evolution.

Other authors are beginning to suggest that some stars can lose their disks quickly (e.g., Silverstone et al. 2006). Recent works (e.g., McCabe et al. 2006; Prato et al. 2003 and references therein) have found pre–main-sequence binary components in different states of disk evolution (such as a Class II paired with a Class III), and in those cases, the evidence for the stars being exactly the same age is much stronger than the circumstantial evidence for the Perseus aggregates. It is therefore plausible that the aggregate members could be coeval and also display a wide range of disk and envelope properties.

In any case, the observational evidence we present here is that objects of at least Class I (if not younger) to at least Class II (if not Class III) are located within close proximity (∼0.1 pc) to each other. Additional multiwavelength follow-up studies of these

groupings of stars in Perseus (and elsewhere) will shed light on the issues raised by this result.

4.2. Objects Detected at All Three MIPS Bands

While there are many objects detected at all four IRAC bands, or even all four IRAC bands plus MIPS-24, there are few objects detected at all three MIPS bands. Objects detected at all three MIPS bands are likely to be quite interesting because they are likely to be the most embedded; moreover, if they are detected at 70 and 160 μm using our observing strategy, they are among the brightest objects in the region and therefore most likely cloud members. In this section we discuss the 16 objects in our catalog detected at all three MIPS bands. Many of these objects have already been discussed (and had SEDs presented) in J06 or above in § 4.1.1. For completeness and ease of reference, all of these objects appear in Table 6 under "objects detected at all three MIPS bands" even if they have already appeared under the "Per 6 aggregate" heading or in J06. Because objects were detected in all three bands throughout our large map, for lack of a better approach, we discuss these objects in approximately right ascension order (the same order as they appear in Table 6), although we start with all of the objects discussed by J06. J06 considered the colors of deeply embedded sources, and several Class I/II objects mentioned there did not have SEDs, so they appear here. The objects are portrayed by position in Figure 13. We investigated the SED and the morphology of each object individually in all our available wavelength regimes (2MASS through 160 μm).

J06 has a discussion of the objects in the L1448 region, including full SEDs of the embedded Class 0 objects (L1448-C and L1448-N) and images of the outflows. The complex morphology here makes it occasionally difficult to extract the point sources from their outflows. L1448-C is clearly broken into two pieces in the IRAC images. L1448 IRS 1 is just off the edge of the four-channel IRAC map and so was not included in detail. The full SED for L1448 IRS 1 (including the two IRAC bands that observed it) is presented for the first time including *Spitzer* points in Figure 23; indeed, it is a deeply embedded object, as expected from earlier observations. Images of this region in all three MIPS bands are striking (see Fig. 24). The southernmost bright 24 μm source in the image is L1448-C (L1448-mm). Where IRAC sees two objects here, only one of which is associated with the millimeter source (J06), MIPS-24 clearly also sees two sources. The object detected at MIPS-70 also appears to be extended. Moving north from this object, we find L1448-N (L1448 IRS 3). MIPS-24 also marginally resolves L1448-N(A) from L1448-N(B); the "B" component is substantially fainter than the "A" component, consistent with results from Ciardi et al. (2003). These objects are not resolved at 70 μm. At 160 μm, all of the IRS 3 components are combined into one saturated blob. Moving westward from L1448 IRS 3, we encounter L1448 IRS 2 and then IRS 1. Both of these objects appear pointlike in MIPS-24 and MIPS-70. There is a slight extension in MIPS-160 toward IRS 3. IRS 1 is faint at MIPS-160, but detected. Because IRS 2 and IRS 3 are at least slightly resolved in at least one band, they do not appear in Table 6; IRS 1 is a point source in all three bands, and so it does appear in the table. IRS 1 is one of the bluest two objects in [24] − [70] colors in Figure 11.

J06 also includes a discussion of objects from L1455, including matching of outflows to driving sources. J06 find the three previously known YSOs (L1455 IRS 1, IRS 2, and IRS 3) but also identify new infrared sources, including one named L1455 IRS 4, a candidate Class I object. IRAS 03235+3004 is also identified in this region as a candidate Class I object. In IRAC, IRS 4 is undetected at the shorter two IRAC bands. SEDs appear for
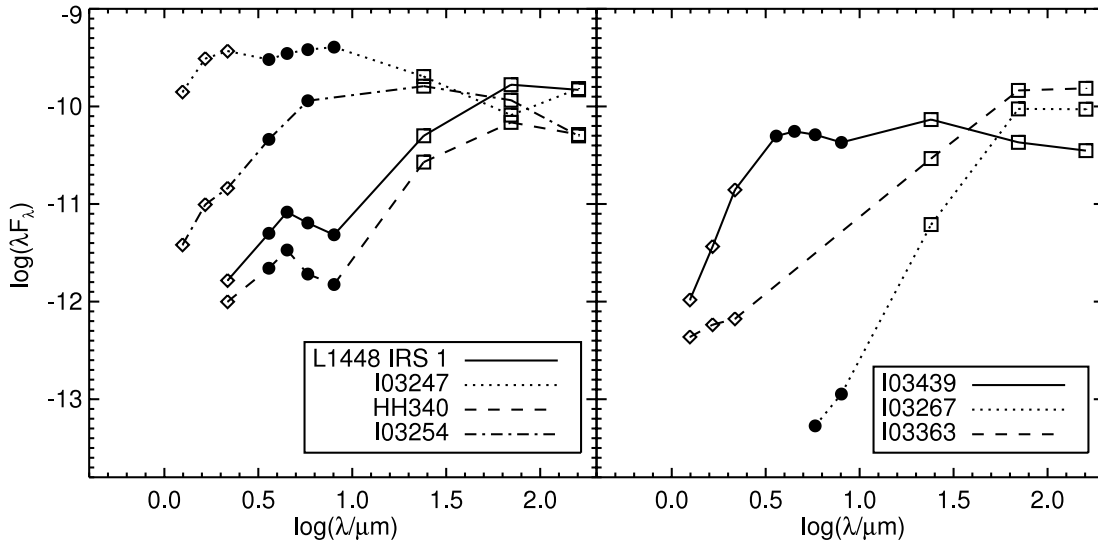
F<small>IG</small>. 23.—SEDs for objects detected at all three MIPS bands and not already discussed elsewhere. Notation is as in Fig. 18. Discussion of each of these objects appears in the text.

both of these objects in J06; both of them are detected at all three MIPS bands and so appear in Table 6. IRAS 03235+3004 is one of the reddest objects in Figure 10 with $K_s - [70] > 15$ mag. L1455 IRS 2 (IRAS 03247+3001) is also seen at all three MIPS bands. This less embedded Class II did not have an SED in J06, and so it appears in Figure 23 (abbreviated "I03247"). IRAS 03247+3001 is one of the bluest two objects in $[24] - [70]$ colors in Figure 11.

The remaining objects detected at all three MIPS bands that are discussed in J06 with SEDs are IRAS 03282+3035 and IRAS 03292+3039, both of which are outflow-driving sources on the B1 ridge. The MIPS flux densities for these candidate Class 0 objects simply appear in Table 6; for SEDs and much more discussion, please see J06. Both of these objects have faint nebulosity around them in at least one of the IRAC bands. For completeness, we note that IRAS 03282+3035 and IRAS 03292+3039 are two of the five reddest objects in Figure 11 with $[24] - [70] > 7$ mag.

Returning to our roughly right ascension order discussion, the next object in Table 6 is IRAS 03254+3050. Another object similar in morphology with detections in all three MIPS bands is

IRAS 03439+3233 (also known as B5 IRS 3). Both of these objects appear to be point sources at all available *Spitzer* bands, both IRAC and MIPS. SEDs for these objects, abbreviated "I03254" and "I03439," respectively, appear in Figure 23. These SEDs are consistent with those for typical Class I sources, and indeed both have already been identified as such in, e.g., Ladd et al. (1993).

Searching in the literature by position for our objects detected at all three MIPS bands, we find one listed as HH 340 (Bally et al. 1996). The SED for this object appears in Figure 23; a multiwavelength image of HH 340 appears in Figure 25. The SED for this object resembles that of the object discussed in § 4.1.1 as being identified with HH 369, with most of the energy being emitted at the longest wavelengths. The overall shape of the SED is also consistent with the flux at the shortest wavelengths being scattered light (such as would be found in edge-on disks). Because we are not aware of jets or knots of ISM alone possessing these properties, we suspected that this object is not truly an HH object, but rather a protostar in its own right, perhaps with shocked emission close to the central object. Indeed, others, including Hodapp et al. (2005), have already come to this same conclusion, that HH 340 is
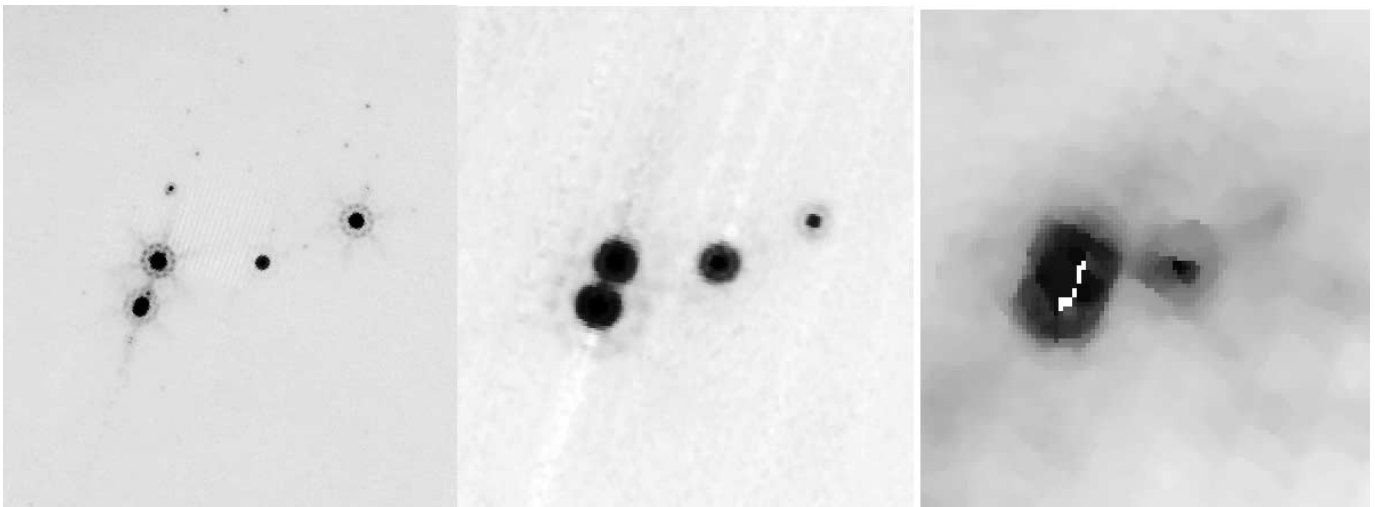

F<small>IG</small>. 24.—L1448 region in all three MIPS bands: 24, 70, and 160 μm, from left to right. See text for discussion.
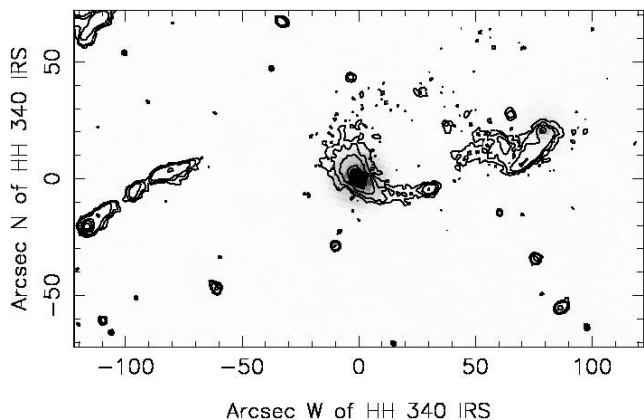
FIG. 25.—Gray-scale MIPS 24 μm image of SSTc2d 032845.3+310541 (HH 340) overlaid by contours of 4.5 μm emission. The contour spacing is a factor of 2 in surface brightness. Scattered light near the source is elongated at a different P.A. from the presumed line emission at greater distances.

actually a jet-driving source. Hodapp et al. (2005) identify the driving source with IRAS 03256+3055; they find a bipolar jet of S-shaped morphology, very similar to that seen in our IRAC images (Fig. 25). Young et al. (2003) identify this object as a Class I. This object and HH 369 appear pointlike in MIPS bands (see Fig. 25) but slightly extended at IRAC bands,[22] consistent with this interpretation. Moreover, this object is located in a region rich with outflows and therefore young, embedded objects, and as such it is reasonable to assume that it could also be a young, embedded object. This object is also one of the reddest dozen objects in Figure 8 with $K_s - [24] > 9.7$ mag, and also one of the reddest objects in Figure 10 with $K_s - [70] > 15$ mag.

One object, IRAS 03267+3128 (abbreviated "I03267" in Fig. 23), has no 2MASS counterpart at all and is only marginally detected, if that, at IRAC-1 and IRAC-2; by eye, it is difficult to see the object in the IRAC images. An SED for this object can be found in Figure 23. It resembles the SED found for IRAS 03282+3035, discussed as an outflow-driving source in J06, and also that for one of the new objects discussed above in § 4.1.1. All of these SEDs steeply rise at the longer wavelengths; the two previously identified in *IRAS* level off between 70 and 160 μm. Because all are faint between 3.5 and 8 μm and undetected in 2MASS, all three are evidently deeply embedded objects. There are clearly outflows in IRAC-2 associated with IRAS 03282+3035, as discussed in J06, consistent with it being a young, embedded object; it is listed as a Class 0 object in Froebrich (2005) (see also, e.g., Barsony et al. 1998 and references therein). The similarities between the morphology at IRAC bands and the SED of this object and IRAS 03267+3128 suggest that IRAS 03267+3128 may also be a Class 0 object.

Returning to our roughly right ascension order discussion, the next three objects in Table 6 are IRAS 03271+3013, IRAS 03273+3018, and a new object (SSTc2d 033032.7+302626). These objects are presented as part of the new Per 6 aggregate discussed above in § 4.1.1.

The next object in the table, SSTc2d 033925.5+321707, with an SED also portrayed in Figure 23 (abbreviated "I03363"), can be identified with 2MASS 03392549+3217070. The source IRAS

03363+3207 is 30″ from this position, with an error ellipse that overlaps the position of our MIPS detection. We therefore conclude that IRAS 03363+3207 probably should be identified with our detection. The shape of its SED is similar to the other young objects discussed here, particularly IRAS 03235+3004, except that it has a faint NIR counterpart where IRAS 03235+3004 does not. This object is located near the north edge of the large emission ring seen in the extended emission, in a region outside the coverage of our IRAC data, but also in a region of relatively low nebulosity in MIPS-24. It is one of the dozen reddest objects in Figure 8 with $K_s - [24] > 9.7$ mag, and also one of the reddest objects in Figure 10 with $K_s - [70] > 15$ mag. This source lies within a small dark cloud about $1.5' \times 2'$ in size, as seen on POSS red plates. It appears to be a single YSO in a relatively isolated cloud core. Follow-up observations are warranted to determine if it is in fact an isolated core.

An object that is bright in all seven *Spitzer* bands is LkHa 330; this object is discussed further in Brown et al. (2007), but it is also included in Table 6 for completeness. It is the bluest object in $[70] - [160]$ colors in Figure 11.

We expected that none of the objects detected in 160 μm would be extragalactic; the sensitivity of our 160 μm survey is such that it is really only likely to probe Galactic objects, e.g., cluster members. The last of the objects detected at all three bands appears to be new (e.g., nothing appears in SIMBAD at that position). It is near the edge of the large MIPS map and has no IRAC coverage; it is identified with source 2MASS 03461106+3308488. It is one of the reddest four sources in $[70] - [160]$ colors in Figure 11. By inspection of the 24 μm image, it is elliptical in MIPS-24 and appears by eye to be a very marginal detection at MIPS-160. Looking at this position in the POSS and 2MASS reveals an extended object that seems likely to be a galaxy. We conclude that *most* of the objects we see at 160 μm, those that are bright and not near the far reaches of the map, are likely to be cloud members.

4.3. *HD 281159* (*BD +31 643*)

HD 281159 (BD +31 643) is a B5 star primarily responsible for illuminating the IC 348 reflection nebula (Witt & Schild 1986) and is a 0.47″ binary (Alzner 1998). Optical coronagraphic images by Kalas & Jewitt (1997) detected a bright linear feature within the IC 348 nebulosity, centered on HD 281159 and with diameter 40″, and suggested that this might be a debris disk seen in scattered light. However, the extent of the linear nebulosity (10,000 AU for $d = 250$ pc) is much larger than the diameters of known debris disks; the nearest *IRAS* source, IRAS 03414+3200, is offset 28″ southeast of the stellar position; and the disk has not been confirmed in subsequent *Hubble Space Telescope* imaging, perhaps because of low surface brightness (P. Kalas 1997, unpublished; HST GO program 7414).

Spitzer's view of the region surrounding HD 281159 is shown in Figure 26. The region has a complex combination of stellar point sources and extended emission, with the stars best seen in the 3.6 μm IRAC image and the extended emission being especially prominent at 24 μm. At lower surface brightness levels, the extended emission has the appearance of an incomplete spherical shell centered on HD 281159, ~200″ (50,000 AU) in diameter and open toward the northwest. Within the shell, there is a narrow spike of very bright 24 μm emission extending from southeast to northwest across the star. This spike is the highest surface brightness feature in the entire Perseus cloud at 24 μm and follows the position angle of the disklike nebulosity found by Kalas & Jewitt (1997). However, the surface brightness distribution along this spike is highly asymmetric about the star.
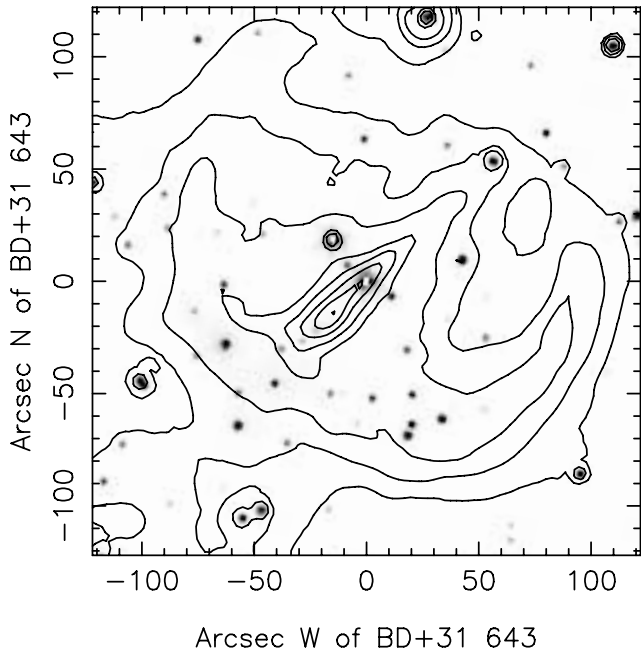
---

[22] Note that flux densities in the IRAC bands for this and other similar objects may not appear in the 2005 c2d catalog at IRAC wavelengths because the objects are extended; flux densities from the 2005 c2d catalog were compared with those obtained using extremely simple aperture photometry to approximate the flux density, and the best apparent value is plotted here and for other similar objects in this discussion.

Fig. 26.—Region of IC 348 centered on the debris disk candidate BD +31 643 (HD 281159). The IRAC 3.6 μm image (see J06) is shown in gray scale, overlaid by contours of MIPS 24 μm emission. The contour intervals are 62, 74, 91, 116, 150, 198, 267, 363, and 500 MJy sr^{-1}.
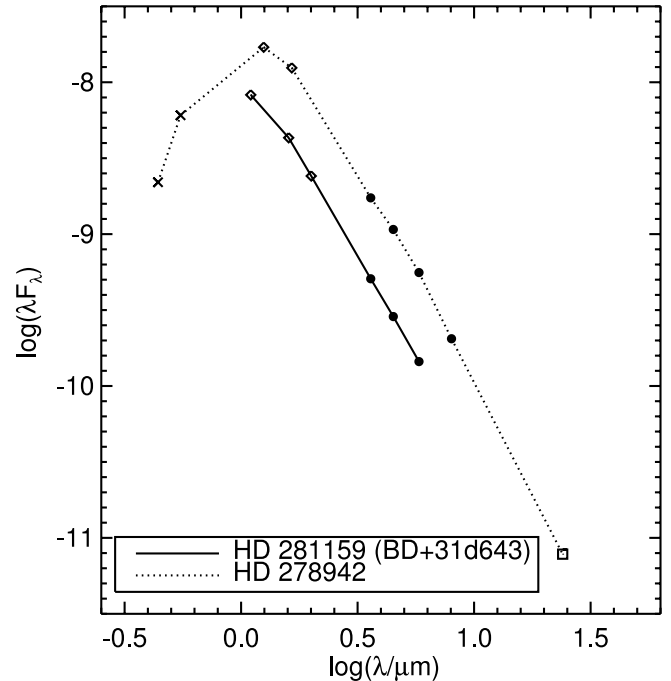

Fig. 27.—SEDs for HD 281159 (BD +31 643; *solid line*) and HD 278942 (*dashed line*). Notation is similar to earlier figures; crosses are optical data, diamonds are 2MASS, filled circles are IRAC, and the square is MIPS-24. Note that BD +31 643 has an upper limit at MIPS-24 that is comparable to the detection for HD 278942. Both stars have a long-wavelength SED completely consistent with a Rayleigh-Jeans slope.

Along the spike, the surface brightness peak is found 22$''$ southeast of the star; at the same distance on the opposite side of the star, the spike feature is ~4 times fainter. At low surface brightness levels, the spike appears to project as far as 80$''$ northwest of the star, but on the southeast side it terminates only 55$''$ away, near the apparent shell wall. The thickness of the spike is spatially resolved at 24 μm, with an FWHM of 14$''$ (3500 AU).

Previous work had suggested an infrared excess in HD 281159. The *Spitzer* SED (Fig. 27) is consistent with a bare stellar photosphere out to 8 μm. There is no point source at 24 μm, to an upper limit of 50 mJy determined by PSF planting (e.g., adding an artificial point source to the MIPS image at the stellar position, and determining the smallest flux normalization at which it remains clearly visible). The source is undetected at 70 μm or in the submillimeter continuum (Enoch et al. 2006). Previous *ISO* SWS observations made in 1997 (Merín 2004) showed a nonnegligible infrared excess starting at ~4 μm. To compare that observation with the *Spitzer* measurements, we convolved the SWS spectrum from the *ISO* Data Archive (TDT 65201414, pipeline ver. 10.1) with the *Spitzer* IRAC and MIPS filter passbands. The *ISO* flux densities are consistent with the *Spitzer* ones except at 8 and 24 μm, where the *ISO* ones are much higher. We attribute the discrepancy to the bright extended emission around the source at 8 and 24 μm (Fig. 26), which should have strongly contaminated the *ISO* measurements in the large 14$'' \times 20''$ entrance aperture of SWS.

The infrared properties of the region around HD 281159 are very difficult to reconcile with a circumstellar debris disk. The star has no clear infrared excess. For a central luminosity of 1600 $L_\odot$, 24 μm thermal emission from a disk should peak at radii near 200 AU, i.e., within 1$''$ of the star. While a spikelike feature corresponding to the proposed disk structure is present at 24 μm, its strong asymmetry is inconsistent with a centrally heated circumstellar disk. The spike feature's length at 24 μm is >3 times larger than its reported optical size, exacerbating the size discrepancy between it and known debris disks. To the southeast, the resolved

thickness of the spike corresponds to an opening angle of 35° as seen from the star, much larger than would be expected for a disk close to edge-on.

What is the distribution of material in the region around HD 281159? An extended disk appears very unlikely in the light of the *Spitzer* results. Nevertheless, the star is still likely to be the illuminating source of the surrounding region in both scattered light and 24 μm emission. HD 281159 is likely another example of a Pleiades-like phenomenon, where an interstellar cloud illuminated by a high-luminosity star mimics some properties of a circumstellar disk. Kalas et al. (2002) report six similar objects. In this case, the star appears to be clearing a cavity in surrounding molecular cloud material. The spike feature would appear to be some kind of filamentary interstellar cloud structure crossing behind or in front of HD 281159 and passing closest to the star on its southeast-projected side. Filamentary structures are expected to form during magnetically mediated collapse of interstellar clouds and can be seen at lower surface brightness levels in other parts of Perseus (such as around HD 278942; see Fig. 28). In the case of HD 281159, such a structure is located very near a luminous star and coincidentally projected across it.

4.4. *HD 278942*

HD 278942 (IRAS 03367+3145) is a B0 V star about 1° west of IC 348. It lies at the center of a large, bright ring of extended MIR emission first identified by *IRAS*. The ring structure is clearly seen in our 24 μm image mosaic and extends well outside the $A_V = 2$ extinction contour used to define the c2d map region (see Figs. 2–5 and 15 and § 3.5). Studies of the ring by Andersson et al. (2000) and Ridge et al. (2006) suggest that it may represent a weak H ɪɪ region excited by HD 278942 and located just behind the Perseus molecular clouds.
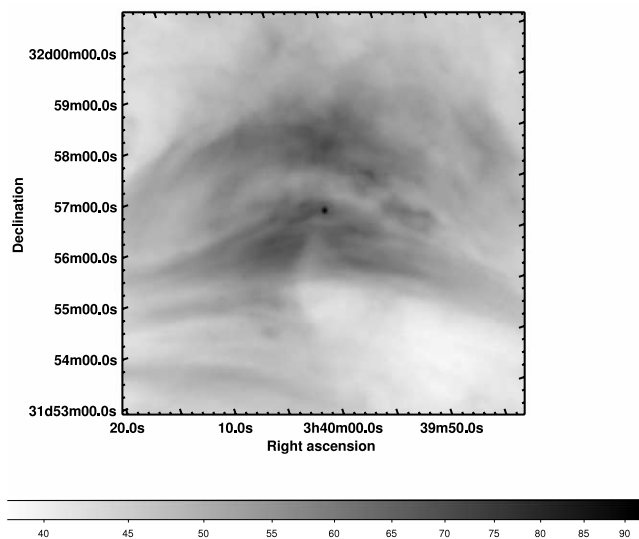
Fig. 28.—Image of HD 278942 at 24 μm, shown in linear stretch. The star appears as a relatively isolated point source, suggesting that it is detached from the material it is illuminating.

Fig. 29.—*Spitzer* image of BD +30 540 at 24 μm, shown in log stretch. The source is nebulous and illuminates an extended emission nebula. The surface brightness units are in MJy sr^{-1}. The vertical image axis corresponds to P.A. = 341.3°.

The 24 μm image of the region (see Fig. 28) shows that HD 278942 lies at the center of a bright striated region of extended emission more than 0.5° in diameter. The emission surrounding this source appears extremely "blue" to MIPS (see Fig. 5), meaning that relative to the rest of the Perseus extended emission, this location is much brighter at 24 μm than at 70 or 160 μm. The star stands out as an isolated point source against this MIR nebulosity; there is no sharp peak in the nebula surface brightness around the stellar position. This "detached" relationship between the star and nebulosity indicates that extended warm dust is not distributed within a filled circumstellar volume. Instead, it appears that the illuminated dust represents a cloud surface that is offset a considerable distance from the star, consistent with previous arguments that HD 278942 lies behind the main Perseus cloud complex.

The bright extended emission surrounding HD 278942 makes it difficult to isolate the stellar fluxes in lower resolution MIR data sets such as *IRAS* and *MSX*. The *IRAS* data suggested a strong 25 μm excess and led Andersson et al. (2000) to suggest that the star possessed a circumstellar debris disk. *Spitzer* flux density measurements, obtained using PSF fitting photometry, are shown as an SED in Figure 27. The star is undetected at 70 and 160 μm and shows a Rayleigh-Jeans spectrum between 3.5 and 24 μm. There is no evidence for an infrared excess from circumstellar dust.

4.5. BD +30 540 and Environs

BD +30 540 (SAO 56444; IRAS 03227+3045) is a B8 V star that illuminates the reflection nebula Van den Bergh 13, 10′ north of L1448. This object is covered by our *Spitzer* MIPS scans but falls outside the region of IRAC coverage (see Fig. 1). As can be seen in Figure 29, the 24 μm image of the region shows that the region around the star is nebulous at this wavelength and immersed in patchy MIR nebulosity extending to distances of 2′ (30,000 AU at 250 pc). Several other point sources are present in the field within ~5′ that have infrared excess:[23] the emission-line

---

[23] We note for completeness that we do not consider this grouping of stars an aggregate of the sort discussed above because it covers a larger area and has larger typical nearest neighbor distances.
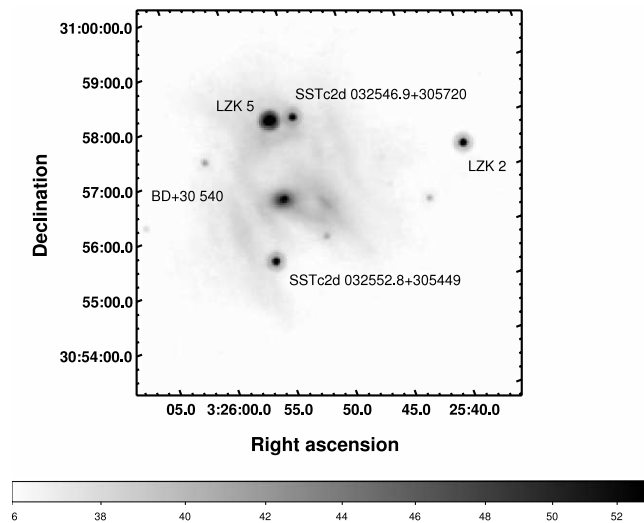
stars LZK 5 (SSTc2d 032548.9+305725, 1.5′ north-northwest of BD +30 540) and LZK 2 (SSTc2d 032533.2+305544, 3.6′ west of BD +30 540); SSTc2d 032546.9+305720, 28″ west of LZK 5; and SSTc2d 032552.8+305449, about 1′ southeast of BD +30 540. BD +30 540, LZK 2, and LZK 5 are also detected at 70 μm. At 24 μm, the star itself is situated on the west side of a compact, elliptical patch of nebulosity that is elongated at P.A. = 80°. Its 24 μm flux density is ~0.1 Jy, consistent with the *IRAS* 25 μm upper limit. Unlike the four nearby stars with infrared excess, which show Class II SEDs, BD +30 540 is a Class I source, one of the reddest objects in Figure 10 with $K_s - [70] > 15$ mag. The 70 μm point source has a flux density of 1.2 Jy, more than a factor of 5 smaller than the *IRAS* 60 μm flux density. The rest of the 70 μm flux density is distributed in bright nebulosity extending 1.6′ to the east of the star at P.A. = 80°; when this is accounted for, the *Spitzer* 70 μm and *IRAS* 60 μm flux densities come into rough agreement. Unfortunately, the 70 μm nebulosity near BD +30 540 is crossed by a strong scan artifact, which prevents any detailed interpretation of its structure.

4.6. HH 211 Outflow and Source

HH 211 is a bipolar outflow on the southwest side of IC 348, originally discovered in NIR H$_2$ emission by McCaughrean et al. (1994). Gueth & Guilloteau (1999) mapped the corresponding CO outflow at high resolution, finding it to be highly collimated. They also detected the central outflow source in the millimeter continuum and derived a circumstellar mass of 0.2 $M_\odot$. NIR spectroscopy of the flow is reported by O'Connell et al. (2005). A wide-field H$_2$ imaging survey of the region by Eislöffel et al. (2003) identified a new north-south-oriented outflow a few arcminutes from HH 211 and suggested that a second bright millimeter continuum source along its axis ("IC 348 MMS") was the driving source. Both of these outflow sources are detected in the centimeter continuum (Avila et al. 2001). Neither has been detected in the NIR, and source confusion in the complex IC 348 field prevented their detection by *IRAS*. MIPS observations, by virtue of their improved sensitivity and spatial resolution over previous far-infrared studies, offer a new opportunity to characterize these two Class 0 outflow sources.
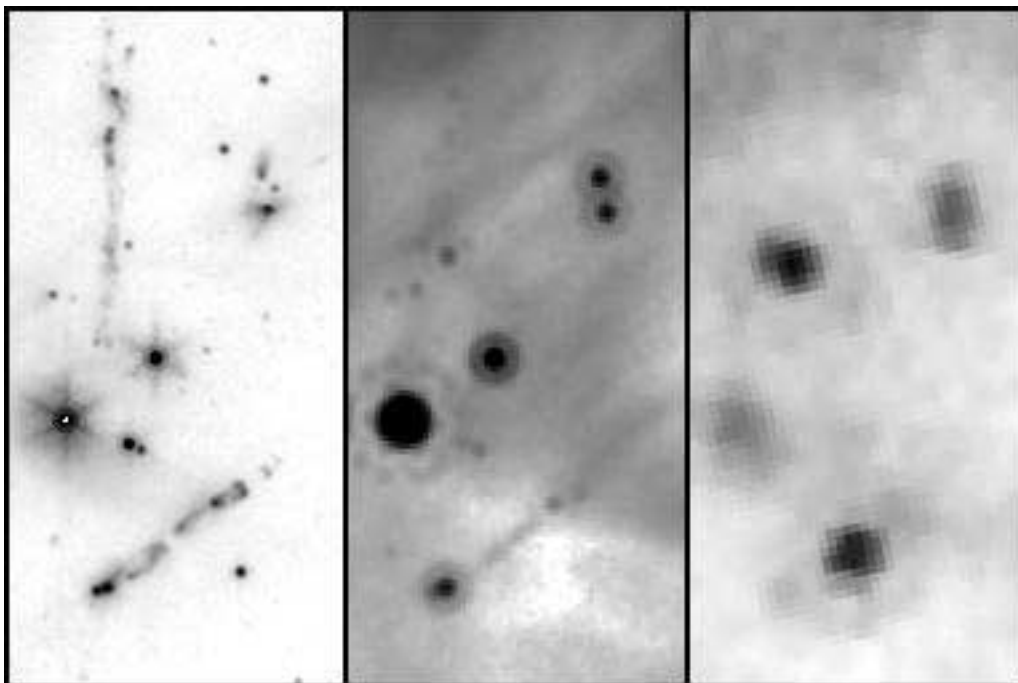
Fig. 30.—*Spitzer* images of the HH 211 field at 4.5, 24, and 70 μm, left to right. This uses a logarithmic stretch for the 4.5 μm image and a linear stretch for the 24 and 70 μm images. The two outflow driving sources are extremely red. The HH 211 jet is detected in the broadband 24 μm image, and its two bow shocks are seen at both 24 and 70 μm.

Spitzer images of the HH 211 field at 4.5, 24, and 70 μm are shown in Figure 30, and a wider field-of-view three-color image is shown in Figure 31. The outflows appear prominently in the IRAC 4.5 μm band, which includes the $S(10)$ and $S(9)$ pure rotational transitions of H_2. The MIR morphology of both flows appears very similar to their NIR vibrational emission (Eislöffel et al. 2003). Neither driving source is detected at any of the IRAC
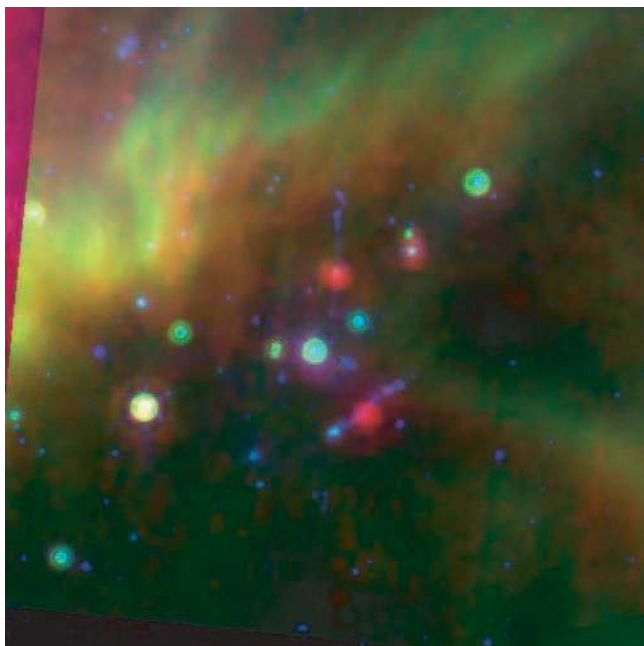

Fig. 31.—*Spitzer* three-color image of the HH 211 field at 4.5 (*blue*), 24 (*green*), and 70 μm (*red*). This uses a logarithmic stretch for the 4.5 μm image and a linear stretch for the 24 and 70 μm images.

bands, unlike the Class 0 objects discussed in J06. At 24 μm, the HH 211 source is still undetected, but several flow features are visible: the narrow bipolar jets; a central gap in the narrow jet at the position of the outflow source; bright emission from the outermost southeast bow shock (knot j, in the nomenclature of McCaughrean et al. 1994); and fainter emission from the northwest bow shocks (knots b/c and e/d). In the other north-south outflow, the driving source is just detected with a flux density of 11 mJy, and faint indications of the north outflow emission are seen. At 70 μm, both driving sources become very bright ($F_\nu \approx$ 3.5 Jy). Both are slightly extended: Gaussian fitting, followed by subtraction in quadrature of the nominal PSF FWHM, finds that the HH 211 source is elongated by $11''$ (2750 AU) at P.A. = $52°$ and that IC 348 MMS is elongated by $13''$ (3250 AU) at P.A. = $125°$. Significantly, both the southeast and northwest bow shocks in HH 211 are detected at 70 μm—the first time individual HH knots have been clearly detected in MIPS 70 μm images. Neither of the two outflow sources can be identified at 160 μm, due to saturation and confusion of bright extended emission in the region. SEDs for both sources are shown in Figure 32.

What is the nature of the far-IR emission from the HH 211 bow shocks? Spectroscopic studies found that continuum emission was negligible near 24 μm in HH 47 (Noriega-Crespo et al. 2004), HH 7 (Noriega-Crespo 2002; Neufeld et al. 2006), and HH 54 (Neufeld et al. 2006). An emission line such as [S I] 25.2 μm might account for the visibility of the flow features in the MIPS 24 μm filter. If so, the line flux corresponding to the 40 mJy flux density measured for the HH 211 southeast bow shock would be 1.3×10^{-15} W m^{-2}, which equates to a luminosity of 2×10^{-4} $L_\odot$ at 250 pc distance. The 70 μm flux densities of the southeast and northwest bow shocks, measured after subtracting the PSF of the central source, are 80 and 20 mJy, respectively. The [O I] line at 63.18 μm is known to be bright in HH flows (Moro-Martín et al. 2001), and the MIPS 70 μm filter has 70%
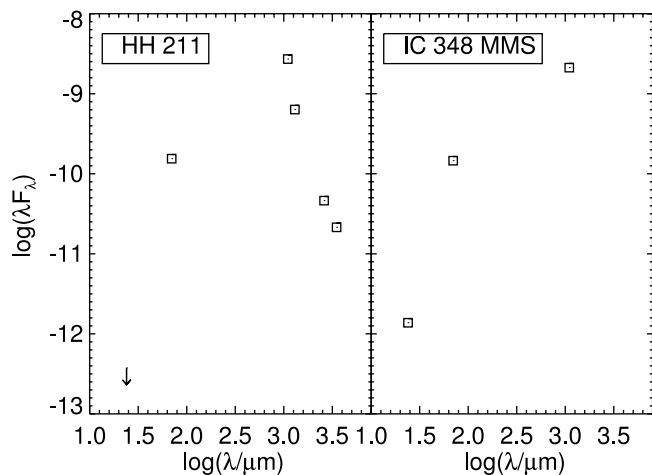
FIG. 32.—SED for HH 211 and IC 348 MMS. Note that most of the points are longer than *Spitzer* wavelengths; only the two shortest wavelength points in HH 211 and the three shortest in IC 348 MMS are *Spitzer* points.

paper we have selected just a few items to highlight from this incredibly rich data set.

Bright extended emission is present at all three wavelengths throughout the MIPS Perseus mosaics. The majority of the extended structures we see have direct counterparts in the *IRAS* maps. At 24 and 70 μm, there is more extended emission on the east side of the complex, where several B stars act as illuminating sources. The distribution of 160 μm emission closely follows the contours of A_V extinction on the west side of the complex. The large 1.4° diameter *IRAS* ring illuminated by HD 278942 does not follow the A_V contours. The structure of the nebulosity immediately surrounding HD 278942 is consistent with a cloud wall illuminated by a star immediately behind it, as suggested for the *IRAS* ring by Ridge et al. (2006).

The source counts found at MIPS 24 and 70 μm are a combination of background galaxies, background and foreground stars, and true cluster members. At 24 μm, in the IC 348 and NGC 1333 clusters, there is a clear excess of cloud member sources for flux densities >2–3 mJy. Across the much larger rest of the cloud region, an excess of on-cloud sources is seen for flux densities >10 mJy. At 70 μm, there is a clear excess above SWIRE of sources obtained at all flux densities >200 mJy in the rest of the cloud and in IC 348; in NGC 1333, an excess in number counts is found for objects brighter than about 65 mJy. The brightest measurable objects in Perseus are found in NGC 1333, where there is a clear excess of these relative to other parts of Perseus.

As a result of observational constraints, the MIPS coverage is about 3 times that of the IRAC coverage. In the region that is covered by IRAC, 92% of the MIPS-24 objects have an IRAC match at some band. The relatively shallow NIR JHK_s data from 2MASS provide some additional data, but only about 30% of the MIPS-24 sources have K_s band counterparts. Nonetheless, one-third of those have MIR excesses, making them potentially cloud members. Many interesting objects throughout this complex have well-defined SEDs.

By making color-magnitude plots using combinations of K_s, 24 μm, and 70 μm, we can make an attempt at separating likely YSOs from likely galaxies such as those found in SWIRE. Many candidate young objects are found throughout the cloud, not just in the well-known clusters; in sheer numbers, there are as many young object candidates outside the clusters as in the clusters. In contrast to J06, we find a much lower frequency of Class I and flat-spectrum sources outside the clusters. The difference can be traced to the selection criteria; by requiring K_s detections, we are implicitly limiting our selection to the brighter objects, and J06 include fainter objects. The MIPS data show that the abundance of *bright* Class I and flat-spectrum sources is not higher in the rest of the cloud versus the NGC 1333 and IC 348 clusters. We find that NGC 1333 is on average younger than IC 348, consistent with expectations.

We find objects that are redder in $K_s - [24]$, $K_s - [70]$, and $[24] - [70]$ than any extragalactic source found in SWIRE at these flux levels; we consider these to be potentially the most embedded young objects, and they are found both in the clusters and in the rest of the cloud.

There are tightly clustered clumps, arcs, and strings of apparently young objects bright at 24 μm located throughout the Perseus cloud. We have presented SEDs and images of the components of a new aggregate called Per 6 and two objects that *IRAS* thought were single point sources but that break into pieces when viewed by MIPS. Each of these groupings of stars has a diversity of SEDs despite being closely colocated (within ~0.1 pc), similar

transmission at this wavelength. If all the 70 μm emission from the southeast bow shock originated in this transition, the implied line flux is 8.9×10^{-16} W m^{-2} (about 10% the value measured in the Cep E bow shocks by Moro-Martín et al. 2001), and the values inferred for the line luminosity would again be $\sim 2 \times 10^{-4}$ $L_\odot$. In this view, the total power emitted in the [S I] and [O I] lines would be comparable to that in the 1–0 $S(1)$ line of H$_2$ at 2.12 μm (McCaughrean et al. 1994). A more speculative possibility is that we have detected dust continuum emission from the bow shock region. In this view, the warm dust would be located in shocked ambient material and in the preshock medium heated by a radiative precursor. The color temperature implied by the measured flux densities is 105 K; a blackbody at this temperature would require an emitting area of $\sim 10^{24}$ m^2, which is comfortably smaller than the MIPS 24 μm beam. The source luminosity would be comparable to the emission-line case. Spectroscopic observations will be needed to distinguish between these two possibilities in the specific case of HH 211. The high implied luminosity of the HH 211 bow shocks, the absence of outer flow features beyond the known bow shocks in the wide-field IRAC maps, and the extremely red driving sources all point toward HH 211 being an extremely young outflow.

The *Spitzer* 70 μm flux densities of the two outflow driving sources are consistent with previously reported *ISO* 60 μm measurements (Froebrich et al. 2003). The new 24 μm measurements provide a strong new constraint on the bolometric temperatures of both objects. Both are among the reddest objects in the entire Perseus cloud, with $[24] - [70]$ color >7 mag. A 30 K blackbody is consistent with the observations of IC 348 MMS and corresponds to an upper limit temperature for HH 211. The low temperatures of the two sources arise from both their dense envelopes and the fact that both are viewed from near the equator plane of their developing circumstellar disks. At 70 μm, the HH 211 source is elongated along the same position angle as in the 1.1 mm continuum (Enoch et al. 2006), 60° from the flow axis and 30° misaligned from the major axis of the circumstellar disk (Palau et al. 2006).

5. CONCLUSIONS

We have presented here the MIPS observations of ~10.5 deg^2 of the Perseus molecular cloud at 24, 70, and 160 μm. In this

to another aggregate found in the Galactic First Look Survey in L1228 (Padgett et al. 2004). This suggests that either (1) all of the objects started with similar properties but at different times such that there is a real age spread and their circumstellar environments today reflect different stages in a process of uniform evolution, or (2) all of the objects are roughly coeval and there is a real diversity of evolutionary states and/or initial conditions. If the former is the case, then some stars are $\lesssim 0.1$ Myr old and some are $\gtrsim 10$ Myr old. If the latter is the case, the evolution of circumstellar matter must be such that the timescale to evolve from Class 0 to Class I is comparable to the shortest possible time to evolve from Class 0 to Class III, and it is perhaps strongly influenced by conditions specific to each star.

There is no real variability of any of the 24 μm sources in our field on timescales of $\sim$6 hr to $\sim$10%.

We used the MIPS data to assess how well the *IRAS* survey did in identifying point sources in a region where complex extended emission is present, posing a significant source of confusion to the large-aperture *IRAS* measurements. Most of the 12 and 25 μm highest quality *IRAS* PSC point sources are retrieved, or it is clear why a point source was reported for that location. There are many more PSC "point sources" reported at 60 and 100 μm (than at 12 and 25 μm); a much lower fraction of these objects are recovered. The *IRAS* FSC is much more robust for studies of stellar sources in regions with complex extended emission and should be used in preference to the *IRAS* PSC unless MIPS data are available.

The 16 objects detected at all three MIPS bands throughout the cloud are expected to be among the most interesting cloud members; they all have colors consistent with embedded young objects, although one on the edge of the field is likely to be a background galaxy (based on POSS observations). We suggest that at least one of these objects may be a new Class 0 object.

Two debris disk candidates, HD 281159 (BD +31 643 in IC 348) and HD 278942, are found not to have infrared excess; *IRAS* measurements suggesting an excess were contaminated by bright extended emission. Two jets in IC 348, HH 211 and IC 348 MMS, are seen at 24 μm; bow shocks are detected at 24 and 70 μm—the first time individual HH knots have been clearly detected in MIPS 70 μm images.

A complete list of candidate young objects in Perseus, along with discussions of clustering and evolutionary timescales, will appear in S.-P. Lai et al. (2007, in preparation).

APPENDIX

IRAS SOURCES NOT RECOVERED BY MIPS

As discussed in § 3.2, we compared the MIPS 24 and 70 μm images and source catalogs with the *IRAS* Point Source (PSC) and Faint Source (FSC) catalogs. A significant number of *IRAS* detections in Perseus are not recovered by *Spitzer* MIPS. The following tables were constructed by overlaying the PSC and FSC source positions on the MIPS 24 and 70 μm images. If an object (or more than one object) appeared at the *IRAS* catalog position, it was marked as having been recovered, even if the MIPS detection was saturated (which happened frequently). If an *IRAS* object was located in a region of bright extended emission in the MIPS image with no immediately obvious point source(s), it was noted that *IRAS* was likely to have been confused by nebulosity. If no MIPS point source was readily discernible at the *IRAS* catalog position, it was marked as missing from the MIPS data. All unconfused *IRAS* 25 μm sources should be recovered in the MIPS 24 μm band, given its greater sensitivity. Similarly, all unconfused *IRAS* 60 μm sources should be recovered in the MIPS 70 μm band. *IRAS* sources that were listed in the *IRAS* catalogs (PSC and FSC) as clear detections (data quality flag of 3) but that are missing in one or both MIPS bands or confused by nebulosity are given in Tables 7 and 8.

Comparing to Table 3, the objects included in Tables 7 and 8 are (1) the 13 PSC objects listed as clear detections at 25 μm but that MIPS-24 reveals are likely to have been simply confused by the nebulosity, (2) the eight PSC objects listed as clear detections at 60 μm but missing entirely from the 70 μm map, (3) the 36 PSC objects listed as clear detections at 60 μm but that MIPS-70 reveals as clumps of nebulosity, (4) the one FSC object listed as a clear detection at 25 μm but that MIPS-24 does not recover at all, and (5) the eight objects listed as clear detections at 25 μm but that MIPS-24 resolves into clumps of nebulosity. No PSC objects are listed as clear *IRAS* detections at 25 μm but are completely missing at 24 μm, and no FSC objects are listed as clear *IRAS* detections at 60 μm. For completeness, we note that one PSC object clearly detected at 12 μm was not recovered at 24 μm (or at 70 μm); it is 03324+3020. A source is present at 24 μm, but offset $\sim 1'$ west of the *IRAS* position. It is reasonably likely that these sources should be matched, but as the positional offset was larger than expected, we have listed it as missing.

TABLE 7
IRAS PSC Detections Not Recovered by *Spitzer* MIPS

PSC Name	From 24 μm	From 70 μm
03265+3014	Missing (listed as upper limit at 12, 25)	Missing (listed as detection at 60)
03292+3124	Confused by nebulosity	Missing (listed as detection at 60)
03303+3108	Confused by nebulosity	Confused by nebulosity
03310+3026	Confused by nebulosity?	Missing (listed as detection at 60)
03313+3117	Confused by nebulosity?	Confused by nebulosity
03319+3044	Confused by nebulosity?	Confused by nebulosity
03323+3049	Confused by nebulosity?	Confused by nebulosity?
03326+3055	Confused by nebulosity?	Confused by nebulosity?
03334+3042	Confused by nebulosity	Confused by nebulosity
03338+3123	Missing (listed as upper limit at 12, 25)	Confused by nebulosity
03346+3116	Confused by nebulosity	Confused by nebulosity
03349+3117	Off edge	Confused by nebulosity
03354+3114	Confused by nebulosity	Confused by nebulosity
03356+3121	Confused by nebulosity	Confused by nebulosity
03358+3138	Confused by nebulosity	Confused by nebulosity
03363+3200	Confused by nebulosity	Missing (listed as detection at 60)
03366+3105	Confused by nebulosity	Missing (listed as detection at 60)
03367+3145	Confused by nebulosity	Confused by nebulosity
03367+3147	Confused by nebulosity	Confused by nebulosity
03367+3147	Confused by nebulosity	Confused by nebulosity
03370+3155	Confused by nebulosity	Confused by nebulosity
03371+3103	Confused by nebulosity	Confused by nebulosity
03371+3135	Confused by nebulosity	Confused by nebulosity
03372+3107	Confused by nebulosity	Confused by nebulosity
03372+3112	Confused by nebulosity	Confused by nebulosity
03374+3056	Confused by nebulosity	Missing (listed as detection at 60)
03380+3114	Confused by nebulosity	Confused by nebulosity
03380+3140	Confused by nebulosity	Confused by nebulosity
03380+3143	Confused by nebulosity	Confused by nebulosity
03382+3145	Confused by nebulosity	Confused by nebulosity
03385+3109	Confused by nebulosity	Confused by nebulosity
03385+3149	Confused by nebulosity	Confused by nebulosity
03386+3206	Confused by nebulosity	Confused by nebulosity
03391+3223	Confused by nebulosity	Confused by nebulosity
03391+3227	Missing (listed as upper limit at 12, 25)	Confused by nebulosity
03404+3156	Confused by nebulosity	Confused by nebulosity
03406+3144	Confused by nebulosity	Confused by nebulosity
03410+3204	Confused by nebulosity	Confused by nebulosity
03411+3155	Confused by nebulosity	Confused by nebulosity
03411+3235	Confused by nebulosity?	Confused by nebulosity
03414+3200	Confused by nebulosity	Confused by nebulosity
03415+3121	Missing (listed as upper limit at 12, 25)	Confused by nebulosity
03417+3159	Confused by nebulosity	Confused by nebulosity
03417+3207	Confused by nebulosity	Confused by nebulosity
03418+3242	Confused by nebulosity?	Missing (listed as detection at 60)
03424+3234	Missing (listed as upper limit at 12, 25)	Confused by nebulosity
03427+3206	Confused by nebulosity?	Confused by nebulosity
03429+3237	Confused by nebulosity?	Confused by nebulosity
03434+3235	Confused by nebulosity?	Confused by nebulosity
03437+3219	Confused by nebulosity	Confused by nebulosity
03439+3131	Off edge	Confused by nebulosity
03448+3302	Confused by nebulosity	Missing (listed as detection at 60)
03449+3240	Confused by nebulosity	Confused by nebulosity
03450+3223	Broken into pieces	Confused by nebulosity
03452+3245	Missing (listed as upper limit at 12, 25)	Confused by nebulosity
03454+3230	Missing (listed as upper limit at 12, 25)	Confused by nebulosity
03455+3242	Confused by nebulosity?	Confused by nebulosity

TABLE 8
IRAS FSC Detections Not Recovered by *Spitzer* MIPS

FSC Name	From 24 μm	From 70 μm
F03345+3116	Confused by nebulosity	Off edge
F03368+3147	Confused by nebulosity	Confused by nebulosity
F03399+3134	Confused by nebulosity	Confused by nebulosity
F03414+3200	Confused by nebulosity	Confused by nebulosity
F03415+3210	Confused by nebulosity	Confused by nebulosity
F03416+3158	Confused by nebulosity	Confused by nebulosity
F03416+3206	Confused by nebulosity	Confused by nebulosity
F03419+3209	Confused by nebulosity	Confused by nebulosity
F03226+3059	Missing (listed as upper limit at 12, solid detection at 25)	Missing (listed as weak detection at 60)

REFERENCES

Alten, V., P., Bally, J., Devine, D., & Miller, G. 1997, in IAU Symp. 182, Herbig-Haro Flows and the Birth of Stars, ed. B. Reipurth & C. Bertout (Dordrecht: Kluwer), 51
Alzner, A. 1998, A&AS, 132, 237
Andersson, B.-G., Wannier, P. G., Moriarty-Schieven, G. H., & Bakker, E. J. 2000, AJ, 119, 1325
Aspin, C. 1992, A&A, 266, 416
Avila, R., Rodriguez, L. F., & Curiel, S. 2001, Rev. Mex. AA, 37, 201
Bachiller, R. 1996, ARA&A, 34, 111
Bally, J., Devine, D., & Reipurth, B. 1996, ApJ, 473, L49
Barsony, M., Ward-Thompson, D., André, P., & O'Linger, J. 1998, ApJ, 509, 733
Beckwith, S. V. W., Henning, T., & Nakagawa, Y. 2000, in Protostars and Planets IV, ed. V. Mannings, A. P. Boss, & S. S. Russell (Tucson: Univ. Arizona Press), 533
Beichman, C. A., et al. 1988, *IRAS* Catalog and Explanatory Supplement
Blum, R. D., et al. 2006, AJ, 132, 2034
Brown, J., et al. 2007, ApJ, submitted
Calvet, N., Briceno, C., Hernandez, J., Hoyer, S., Hartmann, L., Sicilia-Aguilar, A., Megeath, S. T., & D'Alessio, P. 2005, AJ, 129, 935
Cambresy, L., et al. 2006, A&A, 445, 999
Casali, M., & Eiroa, C. 1996, A&A, 306, 427
Chapman, N., et al. 2007, ApJ, submitted
Choi, M. 2005, ApJ, 630, 976
Ciardi, D., Telesco, C., Williams, J., Fisher, R., Packam, C., Pina, R., & Radomski, J. 2003, ApJ, 2003, ApJ, 585, 392
Cieza, L., et al. 2007, ApJ, submitted
de Grijp, M., et al. 1987, A&AS, 70, 95
Eislöffel, J., Froebrich, D., Stanke, Th., & McCaughrean, M. J. 2003, ApJ, 595, 259
Enoch, M. L., et al. 2006, ApJ, 638, 293
Evans, N. J., et al. 2003, PASP, 115, 965
———. 2005, C2D Explanatory Supplement
Fazio, G., et al. 2004, ApJS, 154, 10
Froebrich, D. 2005, ApJS, 156, 169
Froebrich, D., Smith, M. D., Hodapp, K.-W., & Eislöffel, J. 2003, MNRAS, 346, 163
Gordon, K., et al. 2005, PASP, 117, 503
Greene, T., et al. 1994, ApJ, 434, 614
Gueth, F., & Guilloteau, S. 1999, A&A, 343, 571
Hartmann, L. 2003, ApJ, 585, 398
Harvey, P., et al. 2006, ApJ, 644, 307
———. 2007, ApJS, in press
Hatchell, J., et al. 2005, A&A, 440, 151
Hodapp, K., Bally, J., Eisloffel, J., & Davis, C. 2005, AJ, 129, 1580
Jørgensen, J., Johnstone, J., Kirk, H., & Myers, P. 2007, ApJ, 656, 293
Jørgensen, J., et al. 2006, ApJ, 645, 1246 (J06)
Kalas, P., Graham, J. R., Beckwith, S. V. W., Jewitt, D. C., & Lloyd, J. P. 2002, ApJ, 567, 999

Kalas, P., & Jewitt, D. 1997, Nature, 386, 52
Kenyon, S. J., & Hartmann, L. 1995, ApJS, 101, 117
Kirk, H., Johnstone, D., & DiFrancesco, J. 2006, ApJ, 646, 1009
Kraemer, K., et al. 2003, AJ, 126, 1423
Lada, C., et al. 2006, AJ, 131, 1574
Ladd, E., Lada, W., & Meyers, P. 1993, ApJ, 410, 168
Ladd, E., Myers, P., & Goodman, A. 1994, ApJ, 433, 117
Liu, C.-P., Zhang, C.-S., & Kimura, H. 1980, Acta Astron. Sinica, 21, 354
Lonsdale, C. J., et al. 2003, PASP, 115, 897
Makovoz, D., & Marleau, F. 2005, PASP, 117, 1113
McCabe, C., et al. 2006, ApJ, 636, 932
McCaughrean, M. J., Rayner, J. T., & Zinnecker, H. 1994, ApJ, 436, L189
Merín, B. 2004, Ph.D. thesis, Univ. Autonoma de Madrid
Moro-Martín, A., Noriega-Crespo, A., Molinari, S., Leonardo, T., Cernicharo, J., & Sargent, A. 2001, ApJ, 555, 146
Moshir, M., Kopman, G., & Conrow, T. 1992, *IRAS* Faint Source Survey and Explanatory Supplement
Mott, F., & Andre, P. 2001, A&A, 365, 440
Neufeld, D., et al. 2006, ApJ, 649, 816
Noriega-Crespo, A. 2002, Rev. Mex. AA Ser. Conf., 13, 71
———. 2004, ApJS, 154, 352
O'Connell, B., Smith, M. D., Froebrich, D., Davis, C. J., & Eislöffel, J. 2005, A&A, 431, 223
Olmi, L., Testi, L., & Sargent, A. 2005, A&A, 431, 253
Padgett, D., et al. 2004, ApJS, 154, 433
Palau, A., et al. 2006, ApJ, 636, L137
Porras, A., et al. 2007, ApJ, 656, 493
Prato, L., Greene, T., & Simon, M. 2003, ApJ, 584, 853
Rebull, L., et al. 2003, AJ, 125, 2568
———. 2004, AJ, 127, 1029
Reipurth, B., Rodriguez, L., Anglada, G., & Bally, J. 2002, AJ, 124, 1045
Ridge, N., Schnee, S. L., Goodman, A. A., & Foster, J. B. 2006, ApJ, 643, 932
Rieke, G., et al. 2004, ApJS, 154, 25
Silverstone, M., et al. 2006, ApJ, 639, 1138
Skrutskie, M., et al. 2006, AJ, 131, 1163
Strom, K. M., Strom, S. E., & Merrill, K. M. 1993, ApJ, 412, 233
Teixeira, P., et al. 2006, ApJ, 636, L45
Vrba, F., Strom, S., & Strom, K. 1976, AJ, 81, 958
Wainscoat, R. J., Cohen, M., Volk, K., Walker, H. J., & Schwartz, D. E. 1992, ApJS, 83, 111
Wilking, B., et al. 2004, AJ, 127, 1131
Witt, A. N., & Schild, R. E. 1986, ApJS, 62, 839
Yamauchi, S., et al. 2001, PASJ, 53, 885
Yan, J., et al. 1998, AJ, 116, 2438
Young, C., et al. 2003, ApJS, 145, 111
Young, K., et al. 2005, ApJ, 628, 283